

# Optimizing the architecture for coherent beat note acquisition in LISA

Philipp Euringer,<sup>1,\*</sup> Gerald Hechenblaikner,<sup>1</sup> Alexander Sell,<sup>1</sup> Francis Soualle,<sup>2</sup> and Walter Fichter<sup>3</sup>

<sup>1</sup>*Airbus Space Systems, Airbus Defence and Space GmbH,  
Claude-Dornier-Straße, 88090 Immenstaad am Bodensee, Germany*

<sup>2</sup>*Airbus Space Systems, Airbus Defence and Space GmbH,  
Willy-Messerschmitt-Straße 1, 82024 Taufkirchen, Germany*

<sup>3</sup>*University of Stuttgart, Pfaffenwaldring 27, 70569 Stuttgart, Germany*

The laser interferometer space antenna (LISA) senses gravitational waves by measuring distance fluctuations between three spacecraft (SC). These measurements rely on precise tracking of a beat note phase that is formed on a quadrant-photo-diode (QPD) at each SC by interference of a local laser with a laser sent from a distant SC. The crucial prerequisite of the phase tracking is a successful acquisition of the beat note frequency. This article aims to optimize the carrier-to-noise density ratio (CNR) during this process, and to evaluate the resulting probability of detection (PD). CNR is generally lowest during the beat note acquisition process since pointing accuracy relies on coarse acquisition techniques. Based on analytical models, we examine which combinations of QPD segments for the signal read-out yield the highest CNR, i.e., they are least susceptible to pointing errors. We find from simulations that the highest CNR is ensured by taking the maximum of a combination of two segments in vertical and horizontal direction. For pointing errors ( $3\sigma$ ) of  $3.9\ \mu\text{rad}$  and  $4.3\ \mu\text{rad}$  this yields an improvement of around 3.7 dB and 5.6 dB in CNR, respectively, in comparison to a combination of all four segments. In addition, the PD for various configurations of the baselined Fourier peak detection is analyzed. Here we find that the PD is most sensitive to the CNR compared to the design parameters of the acquisition scheme, in particular the FFT length. Moreover, it is shown that aforementioned improvements in CNR can lead to a significant enhancement of the PD.

## I. INTRODUCTION

The laser interferometer space antenna (LISA) is a planned space-based gravitational wave observatory that aims to detect gravitational waves in a measurement bandwidth (BW) from 0.1 mHz to 1 Hz [1]. Detection requires a strain sensitivity of  $10^{-21}$ . This is achieved using a constellation of three SC forming a triangle with a nominal arm length of 2.5 million km. Between each pair of SC two one-way optical links are established in opposing directions. At each of the SC interference of the distant laser with a local one creates a beat note, whose phase fluctuations are proportional to distance fluctuations among the SC. To retrieve the gravitational wave signal the phase of the beat note must be closely tracked via a phase-locked loop (PLL) with a noise floor at  $10\ \text{pm}/\sqrt{\text{Hz}}$ .

However, prior to tracking the links must be acquired first. This is performed in several steps. For the constellation acquisition, a similar approach has been proposed for LISA [2] and TAIJI [3]. It comprises two major phases: (1) spatial acquisition and (2) frequency acquisition. We shall briefly discuss spatial acquisition for one optical link, where SC1 is assumed to transmit a beam towards the receiving SC2. Owing to the large initial uncertainty of the beam pointing (on the order of tens of  $\mu\text{rad}$ ) and the small divergence angle of the laser beam (on the order of a few  $\mu\text{rad}$ ), SC1 cannot directly point its beam towards the presumed location of SC2, as the

beam would almost certainly miss it. Instead, it performs a search spiral in the angular cone of uncertainty. At some point during the spiral scan, the beam “hits” SC2 and is detected by its acquisition sensor (CAS) [2, 4]. SC2 then re-orientes itself towards the direction of the received beam so that its own transmitted beam is detected by the scanning SC1 which in turn re-orientes itself in the direction of SC1. At this point, the beam transmitted from each SC is imaged onto the CAS of the respective opposite SC. Repeating this process for the two other link-pairs concludes the spatial acquisition phase, see e.g. [2, 5, 6]. The probability of success for spatial acquisition primarily depends on the right balance between beam jitter, spiral pitch and beam divergence angle [6]. More refined models also account for the jitter spectrum and its correlation function [7], as well as the scan speed and signal-to-noise ratio of the beam image on the detector [4, 8–11].

Spatial acquisition is followed by frequency acquisition, also referred to as “coherent acquisition”, because a coherent sensor, namely the long-arm interferometer with its QPD sensors, is used to detect the received beam and subsequently lock the PLL, thereby allowing nominal operation of the interferometers [12, 13]. In a first and most critical step, which is the primary focus of this paper, the beat note between the received beam and a local reference beam must be detected. This can only be accomplished if the relative frequency between the two beams, referred to as “heterodyne frequency”, lies within the bandwidth of the phasemeter used for interferometric detection. However, the relative frequency is only known to an accuracy on the order of 100 MHz due to the uncertainties of ground-to-orbit and of Doppler frequency shifts induced

\* philipp.euringer@airbus.com

by the orbital dynamics. This requires a scan of the local oscillator frequency over the entire frequency uncertainty range. At the end of this scan the beat note is detected by a maximum peak search as described in section III A. In a second step, which is less critical and represents no major technical challenge, the PLL is locked after initializing its internal numerically controlled oscillator (NCO) with the heterodyne frequency found in the previous step. At this point, the phase can be read from each of the 4 QPD segment channels and differential wavefront sensing (DWS) [3, 14] can be used to stabilize the pointing with a precision on the order of a few nanorad [2, 13]. Finally, a delay-locked-loop (DLL) is activated to obtain inter-SC ranging information and extract the incoming data stream from PRN code sequences modulated onto the carrier frequency [15–17].

Considerable efforts have been dedicated to the beat note acquisition process itself [12, 18] and to various optimization schemes [19–21]. However, the read-out scheme at the QPD has received very little attention in this context. This, however, is of particular importance since it is well known that the CNR of the beat note strongly depends on the angle of incidence of the interfering laser due to its linear dependence on the heterodyne efficiency [22–24]. During the beat note acquisition, the angle of incidence of the distant laser is enlarged by pointing errors of receiving and transmitting SC. During nominal operation, these pointing errors are minimized via DWS, which, however, is not applicable during the beat note acquisition as it requires coherent tracking. Consequently, we are aiming for a read-out scheme that is least susceptible to pointing errors and thus maximizes the CNR. This is the central point of the presented analysis.

Based on a careful analysis of the heterodyne efficiency on the pointing error of the receiving SC, we show that the maximum heterodyne efficiency of two single segments surpasses the heterodyne efficiency of two segments combined along any axis of the QPD. Moreover the heterodyne efficiency is always most susceptible to pointing errors when all four segments are combined. For these three configurations, the sensitivity of the CNR to pointing errors of transmitting and receiving SC is analyzed. We show that a suitable selection of the configuration can increase the minimum CNR during the beat note acquisition by up to 5.6 dB. In addition, we provide an evaluation of the current beat note acquisition scheme and show that the improvement in CNR can result in a significant enhancement of the PD.

The paper is divided in two parts. Section II is dedicated to the analysis of the CNR. In section II A a general model for the CNR analysis is introduced. To this end, reasonable assumptions are taken into account to allow separate evaluation of parameters affected by pointing errors of the transmitting and the receiving SC. First, pointing errors of the transmitting SC in terms of the received power are analyzed in section II B. Pointing errors of the receiving SC are analyzed in section II C based on the heterodyne efficiency, which naturally leads to the

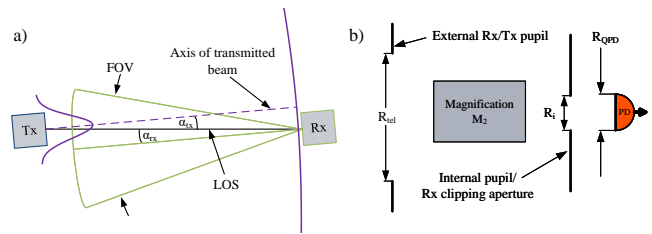


Figure 1. In a) transmitting ('Tx') and receiving ('Rx') SC are depicted by gray boxes. The field of view (FOV) of the receiving SC is depicted by the green cone. The deviation of the FOV center line to the line of sight (LOS) is indicated by the angle  $\alpha_{tx}$ . Purple lines indicate the intensity profile of the distant laser close to the transmitting SC and at the reception of the receiving SC. The deviation of the axis of the transmitted beam to the LOS is indicated by the angle  $\alpha_{tx}$ . In b) the apertures in the receive and transmit path are identified. The photodiode is indicated with 'PD'.

definition of three different read-out configurations. After a discussion of relevant noise contributions in section II D, the CNR of the three configurations in terms of pointing errors of receiving and transmitting SC is analyzed in section II E.

Section III analyses the influence of the CNR on the beat note acquisition scheme. The basic principle and model assumption on the beat note acquisition scheme are described in section III A. In section III B an analysis on the PD is performed. A discussion of the analysis and the implementation of the configurations follows in section III C.

## II. CNR DURING BEAT NOTE ACQUISITION

### A. Generic model

Spatial acquisition of LISA has been completed once each of the six lasers is detected at the center of the CAS of the adjacent SC. The pointing accuracy is represented by random variables  $\alpha$  and  $\beta$  for the angle in constellation plane and out of constellation plane, respectively. For completeness, these and all subsequently defined parameters are listed in Tab. I. If not otherwise specified these parameters are assigned with values listed in [25], thus providing a LISA-representative evaluation.

In general, each laser link is affected by the pointing error of the transmitting SC (denoted via subscript 'tx') and the receiving SC (denoted via subscript 'rx'), leading to four angles  $\alpha_{tx}, \beta_{tx}, \alpha_{rx}$  and  $\beta_{rx}$ , for each laser link. The transmitting angles define which portion of the light cone is present at the receiving SC, whereas both, receiving and transmitting angles, define the angle of incidence at the receiving SC, see Fig. 1 a). The  $3\sigma$  values of  $\alpha_{tx}, \beta_{tx}, \alpha_{rx}$  and  $\beta_{rx}$  are assumed to be identical and are assigned with the values listed in Tab. II. The CNR of 61 dB-Hz, listed in [26], as the lower limit for DWS, has

Table I. Parameter definition

Symbol	Unit	Description
$a_{1o,1f}, a_{s,1f}$	$1/\sqrt{\text{Hz}}$	1f-RIN of local oscillator/signal beam
$C$	$\text{V}^2$	carrier power
CNR	Hz	carrier-to-noise density ratio
$dS$	$\text{m}^2$	surface element
$d_{sc}$	m	inter-SC distance
$E_{1o}, E_s$	$\text{V}/\text{m}^2$	electric field of local/signal beam
$E_{1o}^0, E_s^0$	$\text{V}/\text{m}^2$	amplitude of local/signal beam
$F_{\text{CNR},\text{lim}}$	-	worst-case CNR
$f_s$	Hz	sampling rate
$f_{\text{res}}$	Hz	frequency resolution of FFT
$k_{1o}, k_s$	rad/m	wave number of local/signal beam
$K, K_{\text{tot}}$	-	number of bins/total bins per acquisition
$L$	-	number of samples per FFT
$M$	-	number of FFT intervals
$M_2$	-	total magnification on QPD
$m_{sb}$	rad	sideband modulation index
$N_0$	$\text{V}^2/\text{Hz}$	one-sided Noise PSD
$N_{\text{QPD}}$	-	number of combined QPDs
$N_s$	-	number of segments combined per QPD
$n_{\text{scans}}$	-	number of scans
$P_{1o}, P_s$	W	power of local/signal beam at QPD
$P_{s,n}$	W	nominal received power
$P$	W	power at the QPD
$P_D, P_{D,n}$	-	PD with/without sidebands
$P_s$	W	power of signal beam at QPD
$R_{\text{min}}$	m	$\min(R_{\text{tel}}/M_2, R_{\text{QPD}}, R_i)$
$R_i, R_{\text{tel}}$	m	internal/external pupil radius
$R_{\text{QPD}}$	m	radius of detector area
$S_{\text{bin}}$	$\text{V}^2$	bin power
$s_{\text{I,seg,el}}$	A	current noise density of QPD electronics
$W_0$	m	$1/e^2$ radius of local beam on QPD
$x, y, z$	m	axes of the optical reference frame
$x_s, y_s, z_s$	m	axes of the signal reference frame
$z_0$	m	Rayleigh range
$\alpha, \beta$	rad	angle in/out of constellation plane at QPD
$\alpha_{\text{rx}}, \beta_{\text{rx}}$	rad	angle in/out of constellation plane at Rx SC
$\alpha_{\text{tx}}, \beta_{\text{tx}}$	rad	angle in/out of constellation plane at Tx SC
$\gamma_{\text{max}}$	rad	magnitude of $\alpha_{\text{rx}}$ and $\beta_{\text{rx}}$
$\gamma_{\text{tx}}$	rad	magnitude of $\alpha_{\text{tx}}$ and $\beta_{\text{tx}}$
$\eta_{\text{carrier}}$	-	portion of optical power in main carrier
$\eta_{\text{het}}$	-	heterodyne efficiency
$\eta_{\text{resp}}$	A/W	responsivity of QPD
$\eta_{\text{wfe}}$	-	wave front error
$\lambda_s$	m	wavelength of signal beam
$\delta$	-	non-centrality parameter
$\delta_{\text{main}}, \delta_{\text{sb}}$	-	$\delta$ for main/sideband beat note
$\sigma_{\text{bin}}^2$	$\text{V}^2$	variance of noise bin
$\phi$	rad	radial angle
$\varphi_t, \varphi_i$	rad	total/interferometric phase of beat note
$\omega_{1o}, \omega_s$	rad/s	angular frequency of local/signal beam

Table II. Pointing error of angles  $\alpha_{\text{tx}}, \beta_{\text{tx}}, \alpha_{\text{rx}}$  and  $\beta_{\text{rx}}$ 

Option	$3\sigma$
1	$3.9 \mu\text{rad}$
2	$4.3 \mu\text{rad}$

been used to derive a value of  $3.9 \mu\text{rad}$  ( $3\sigma$ ) for the tolerable angular uncertainty. Option 2 assumes a slightly more robust DWS operation with respect to option 1. At the QPD, the beam of the distant SC interferes with a beam of the local SC. We will denote them as signal beam and local oscillator beam, respectively. The signal beam enters the receiving SC through the telescope with radius  $R_{\text{tel}}$ , see Fig. 1 b). Since transmitting and receiving SC are separated by  $\sim 2.5$  million km, the wavefront curvature is negligible and the intensity distribution is flat so that the received beam is well described by a plane wave over the limiting aperture of the telescope. Consequently, in this case, the complex electric field of the signal beam (indicated via subscript 's'), in its local coordinate system, denoted as signal reference frame (SRF), reads as

$$E_s = E_s^0(\alpha_{\text{tx}}, \beta_{\text{tx}}) e^{ik_s z_s} e^{-i\omega_s t}. \quad (1)$$

Hereby,  $\omega_s$  denotes the angular frequency and  $k_s$  ( $\approx 2\pi/1064 \text{ rad nm}^{-1}$ ) the wave vector of the signal beam. We note that based on the beam characteristics, the transmitted beam angles  $\alpha_{\text{tx}}$  and  $\beta_{\text{tx}}$  only affect the amplitude  $E_s^0$ . The local oscillator beam incident at the QPD is modeled as a Gaussian beam. Its complex representation in paraxial approximation reads as [27]

$$E_{1o} = E_{1o}^0 \exp\left(-\frac{x^2 + y^2}{W^2(z)}\right) \cdot \exp\left(ik_{1o}z + ik_{1o}\frac{x^2 + y^2}{2R(z)} - i\zeta(z) - i\omega_{1o}t\right), \quad (2)$$

with

$$\begin{aligned} W(z) &= W_0 \sqrt{1 + (z/z_0)^2}, \\ R(z) &= z [1 + (z_0/z)^2], \\ \zeta(z) &= \text{atan}(z/z_0), \\ W_0 &= \sqrt{\lambda z_0/\pi}. \end{aligned}$$

The parameter  $\omega_{1o}$  denotes the angular frequency and  $k_{1o}$  ( $\approx 2\pi/1064 \text{ rad nm}^{-1}$ ) the wave vector of the local beam. Amplitude and Rayleigh range are denoted as  $E_{1o}^0$  and  $z_0$ , respectively. The local oscillator beam is expressed in the optical reference frame (ORF) with associated coordinates  $(x, y, z)$ . For the ongoing analysis we assume that the QPD is perfectly aligned with the optical axis of the receiving SC, i.e. with the ORF. We set the origin of the ORF at the center of the QPD as indicated in Fig. 2. Moreover, we assume that the local oscillator beam is perfectly aligned and focused on the QPD, as evident

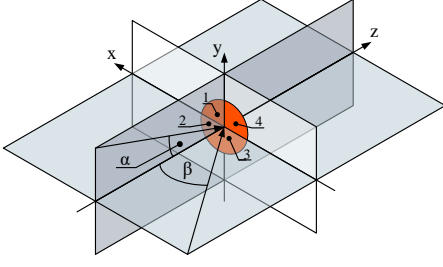


Figure 2. Definition of the ORF and angles  $\alpha$  and  $\beta$ . The QPD is illustrated by an orange circle, where the segments are indicated.

from Eq. 2.

To express Eq. 1 in the ORF, no translation along the  $x$  and  $y$ -axis needs to be considered thanks to its beam characteristics. Moreover, the rotation around the  $z$ -axis is ignored due to axial symmetry. Consequently,

$$\begin{bmatrix} x_s \\ y_s \\ z_s \end{bmatrix} = \begin{bmatrix} \cos \beta & 0 & \sin \beta \\ 0 & 1 & 0 \\ -\sin \beta & 0 & \cos \beta \end{bmatrix} \begin{bmatrix} 1 & 0 & 0 \\ 0 & \cos \alpha & -\sin \alpha \\ 0 & \sin \alpha & \cos \alpha \end{bmatrix} \begin{bmatrix} x \\ y \\ z \end{bmatrix} + \begin{bmatrix} 0 \\ 0 \\ d_{sc} \end{bmatrix} \quad (3)$$

relates the ORF to the SRF. The angles  $\alpha$  and  $\beta$  are indicated in Fig. 2 and represent the angle of the wave vector of the incident plane wave projected onto the  $y$ - $z$  plane and  $x$ - $z$  plane, respectively. These angles are expressed relative to the inertial (on-sky) coordinate system by division with the magnification  $M_2$ , which establishes the relation  $\alpha_{rx} = \alpha/M_2$  and  $\beta_{rx} = \beta/M_2$ . The distance between the SC is denoted as  $d_{sc}$ .

Inserting Eq. 3 in Eq. 1, allows us to write the signal beam as a function of the angles  $\alpha_{tx}$ ,  $\beta_{tx}$ ,  $\alpha_{rx}$  and  $\beta_{rx}$ . To express the signal beam at the reception of the QPD the limiting aperture needs to be taken into account, which is incorporated as follows

$$\begin{aligned} E_s(\alpha_{tx}, \beta_{tx}, \alpha_{rx}, \beta_{rx}) = & \\ \theta(R_{\min} - \sqrt{x^2 + y^2}) E_s^0(\alpha_{tx}, \beta_{tx}) e^{-i\omega_s t} & \\ \cdot \exp(ik_s(-x \sin(M_2 \beta_{rx}) + y \sin(M_2 \alpha_{rx}) \cos(M_2 \beta_{rx}))) & \\ \cdot \exp(ik_s(z \cos(M_2 \alpha_{rx}) \cos(M_2 \beta_{rx}) + d_{sc})) & \end{aligned} \quad (4)$$

with

$$R_{\min} := \min(R_{tel}/M_2, R_{QPD}, R_i).$$

Here, the Heaviside step function  $\theta$  takes into account the clipping of the signal beam by the receiving optic. According to Fig. 1 b), the beam diameter is either limited by the ratio of the telescope aperture with radius  $R_{tel}$  and the magnification  $M_2$ , the internal pupil with radius  $R_i$  or the detector area with radius  $R_{QPD}$ . Using Eq. 4 and Eq. 2, we can then express the optical power  $P$  at the QPD resulting from the electrical field of signal and

Table III. Segment combinations

Label	$x^-$	$x^+$	$y^-$	$y^+$
seg 1	0	$\sqrt{R_{\min}^2 - y^2}$	0	$R_{\min}$
seg 2	0	$\sqrt{R_{\min}^2 - y^2} - R_{\min}$	0	0
ver	0	$\sqrt{R_{\min}^2 - y^2} - R_{\min}$	$R_{\min}$	$R_{\min}$
hor	$-\sqrt{R_{\min}^2 - y^2}$	$\sqrt{R_{\min}^2 - y^2}$	0	$R_{\min}$
all	$-\sqrt{R_{\min}^2 - y^2}$	$\sqrt{R_{\min}^2 - y^2} - R_{\min}$	$R_{\min}$	$R_{\min}$

local oscillator beam

$$\begin{aligned} P &= \frac{1}{2} c \epsilon_0 \iint |E_s(\alpha_{tx}, \beta_{tx}, \alpha_{rx}, \beta_{rx}) + E_{lo}|^2 dS \\ &= \frac{N_s}{4} P_s(\alpha_{tx}, \beta_{tx}) + \frac{N_s}{4} P_{lo} \\ &+ c \epsilon_0 \Re \left( \iint E_s^*(\alpha_{tx}, \beta_{tx}, \alpha_{rx}, \beta_{rx}) E_{lo} dS \right). \end{aligned} \quad (5)$$

Hereby,  $c$  denotes the speed of light and  $\epsilon_0$  the vacuum permittivity.  $E_s^*$  represents the complex conjugate of  $E_s$ . Note that the surface element  $dS = dx dy$  is integrated over an area (specified by integral boundaries) that corresponds to either a single segment or combinations thereof. As will be seen in section II C, for the ongoing analysis, of most relevance are single segments, the combination of two adjacent segments, and the combination of all four segments. Due to symmetry, segment 1 (denoted with subscript 'seg 1') yields the same CNR as segment 3 and similarly, segment 2 (denoted with subscript 'seg 2') equals segment 4. In addition, the vertical combination of segment 1 and segment 2 (denoted with subscript 'ver') yields the same CNR as the combination of segment 3 and segment 4. Similarly, the horizontal combination of segment 1 and segment 4 (denoted with subscript 'hor') is identical to the combination of segment 2 and segment 3. Finally, taking into account the combination of all four segments (denoted with subscript 'all') leaves five different segment and segment combinations. These are specified via their integral boundaries in Tab. III, where columns indicated with  $x^\pm$  and  $y^\pm$  denote the upper (+) and lower (-) integral bounds. In the following, the label will be attached as subscript to parameters and integral bounds to indicate the respective segment (combination). In the second line of Eq. 5 we considered that the optical power of the individual beams  $P_{s/lo} := \frac{1}{2} c \epsilon_0 \iint |E_{s/lo}|^2 dS$  is rotationally symmetric. Therefore, the power only depends on the number  $N_s$  of QPD segments considered for the readout but not on the explicit segments. Only the last term, which is formed by the real part  $\Re$  of the interfering signal, explicitly depends on the choice of the segments. This oscillating term, commonly known as beat note, is usually expressed in terms of the heterodyne efficiency  $\eta_{het}$  defined according to [28]

$$\sqrt{\eta_{het}} e^{-i\varphi_t} := \frac{\iint E_s^*(\alpha_{tx}, \beta_{tx}, \alpha_{rx}, \beta_{rx}) E_{lo} dS}{\sqrt{\iint |E_s|^2 dS \iint |E_{lo}|^2 dS}}. \quad (6)$$

The phase  $\varphi_t = (\omega_s - \omega_{lo})t + \varphi_i$  constitutes the total phase that is formed by the beat note of distant and local laser as well as the interferometric phase  $\varphi_i$ . Consequently, only the last term in Eq. 5 represents the signal of interest. As shown in appendix A (Eq. A3), inserting the explicit expressions of the signal beam (Eq. 4) and the local oscillator beam (Eq. 2) in Eq. 6, the heterodyne efficiency can be expressed as

$$\eta_{\text{het}} = \left| \frac{2}{N_s} \frac{N(R_{\text{QPD}}/W_0)}{W_0 R_{\text{min}} \pi} E_{\text{rl}}(M_2 \alpha_{\text{rx}}, M_2 \beta_{\text{rx}}) \right|^2 \quad (7)$$

with

$$E_{\text{rl}}(\alpha, \beta) := \iint \exp\left(-\left(y^2/W_0^2 + ik_s y \sin(\alpha) \cos(\beta)\right)\right) \cdot \exp\left(-\left(x^2/W_0^2 - ik_s x \sin(\beta)\right)\right) d\tilde{S}, \quad (8)$$

$$N(x) := 2^{3/2} \left(1 - e^{-2x^2}\right)^{-1/2}.$$

Hereby,  $d\tilde{S}$  indicates that, in contrast to  $dS$ , integration is only performed over the area that is not clipped by the aperture with radius  $R_{\text{min}}$ . We note that Eq. 7 only depends on the angles of the received beam  $\alpha_{\text{rx}}$  and  $\beta_{\text{rx}}$  but not on  $\alpha_{\text{tx}}$  and  $\beta_{\text{tx}}$ . In a similar way this can also be shown for the phase  $\varphi_t$ . Finally, using the relation, given by Eq. 6, between the heterodyne efficiency of Eq. 7 and the interference term of Eq. 5, we can rewrite Eq. 5 after some re-arrangements and using Euler's formula as follows:

$$P = \frac{N_s}{4} (P_s(\alpha_{\text{tx}}, \beta_{\text{tx}}) + P_{\text{lo}}) + \frac{N_s}{4} 2\sqrt{P_s(\alpha_{\text{tx}}, \beta_{\text{tx}})P_{\text{lo}}}\sqrt{\eta_{\text{het}}(M_2 \alpha_{\text{rx}}, M_2 \beta_{\text{rx}})} \cdot \cos((\omega_s - \omega_{lo})t + \varphi_i(M_2 \alpha_{\text{rx}}, M_2 \beta_{\text{rx}})). \quad (9)$$

A similar expression has also been found in [24]. The last term in Eq. 9 represents the beat note signal between signal and local oscillator beam. This signal is then converted to a photovoltage signal using a transimpedance amplifier. Based on Eq. 9 it is then straightforward to show that the beat note power  $C$  of this photovoltage signal is given by

$$C = 2 \left( \frac{\eta_{\text{carrier}} \eta_{\text{resp}} N_s N_{\text{QPD}}}{16} \right)^2 \cdot P_s(\alpha_{\text{tx}}, \beta_{\text{tx}}) P_{\text{lo}} \eta_{\text{wfe}} \eta_{\text{het}}(M_2 \alpha_{\text{rx}}, M_2 \beta_{\text{rx}}). \quad (10)$$

Equation 10 accounts for the efficiency of the QPD via the responsivity  $\eta_{\text{resp}}$  and the fact that the signal may be combined from  $N_{\text{QPD}}$  QPDs. In addition, it is considered that parts of the carrier are modulated and therefore only  $\eta_{\text{carrier}}$  of the beat note can be used for the phase read-out [16, 29]. Moreover,  $\eta_{\text{wfe}}$  is an additional constant factor accounting for wavefront errors. A numerical analysis on the wavefront errors including a LISA representative value has been provided in [30]. Importantly, Eq. 10 allows a separation of the angle pairs  $\alpha_{\text{rx}}$  and  $\beta_{\text{rx}}$ , which affect  $\eta_{\text{het}}$ , from the angle pairs  $\alpha_{\text{tx}}$  and  $\beta_{\text{tx}}$ , which determine the received power of the signal beam  $P_s$ . Based on

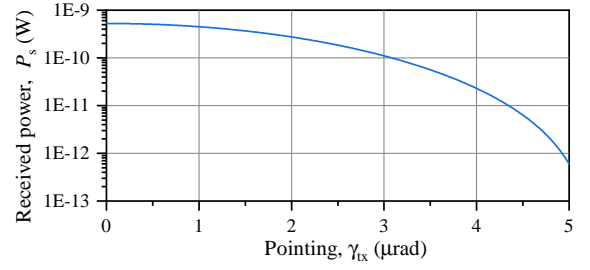


Figure 3. Received Power under variation of the pointing angle  $\gamma_{\text{tx}}$ .

this separation, the sensitivity of the received power on the pointing error of the transmitting SC and the sensitivity of heterodyne efficiency on the pointing error of the receiving SC will be examined in the subsequent sections.

## B. Angle dependence of received power

Each laser serves as local oscillator for the long-arm interferometer of the local OB and as signal beam for long-arm interferometer of the adjacent SC. The signal beam leaves the remote SC through the optics shown in Fig. 1 b). Consequently, the complex electric field of the signal beam in its local coordinate system equals Eq. 2 by changing the beam waist and the laser frequency, which must be different for the interfering beams. In particular, we make the following substitutions  $W_0 \rightarrow W_0 M_2$ ,  $k_{\text{lo}} \rightarrow k_s$  and  $\omega_{\text{lo}} \rightarrow \omega_s$ . The power  $P_s(\alpha_{\text{tx}}, \beta_{\text{tx}})$  of the signal beam received at the local SC can be estimated using the Fraunhofer approximation. This approximation is well suited due to the large distance between the SC. We note that dedicated models for wave front errors or effects due to optical aberration are not considered in this model. Instead, these effects will be considered via constant loss factors, which account for a nominal performance degradation of these effects. Following the derivation of Appendix C, the power  $P_s$  received through an aperture with radius  $R_{\text{tel}}$  at a distance  $d_{\text{sc}}$  is then given by

$$P_s(\gamma_{\text{tx}}) = 2P_{\text{s,n}} \left( \frac{k_s R_{\text{tel}}^2}{d_{\text{sc}}} \right)^2 F^2 \left( \frac{R_{\text{tel}}}{W_0 M_2}, k_s R_{\text{tel}} \gamma_{\text{tx}} \right) \quad (11)$$

with

$$F(r, \kappa) := r \int_0^1 \rho e^{-r^2 \rho^2} J_0(\kappa \rho) d\rho$$

where,  $J_0$  denotes the zero order Bessel function. We note that the received power only depends on the magnitude of the combined angle  $\gamma_{\text{tx}} = \sqrt{\alpha_{\text{tx}}^2 + \beta_{\text{tx}}^2}$ . The parameter  $P_{\text{s,n}}$  denotes the nominal power and accounts for losses in the on-board transmit and receive path. Figure 3 depicts the power  $P_s$  under variation of the angle  $\gamma_{\text{tx}}$ . A

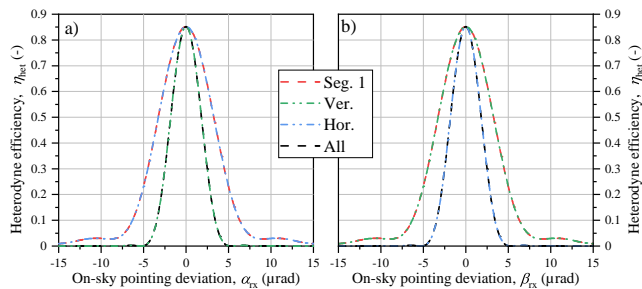


Figure 4. The heterodyne efficiency  $\eta_{\text{het}}$  as a function of angles  $\alpha_{\text{rx}}$  and  $\beta_{\text{rx}}$  is shown in a) and b), respectively. Red lines show the heterodyne efficiency for a single segment, specifically for segment 1. The green curves depict the heterodyne efficiency once the read-out of segment 1 and segment 2 are combined, while the light blue curves combine segment 1 with segment 4. Finally, the resulting heterodyne efficiency once all four segments are combined is depicted by the black lines.

minimum of the received power is observed at around  $5.3 \mu\text{rad}$ .

### C. Angle dependence of the heterodyne efficiency

According to Eq. 7 and Eq. 8, the heterodyne efficiency explicitly depends on the segments considered for the read-out of the beat note. In the following we want to analyze the sensitivity of the heterodyne efficiency on the receiving angles  $\alpha_{\text{rx}}$  and  $\beta_{\text{rx}}$  taking into account different QPD segments for the read-out. To this end, we will omit effects resulting from the finite slit size separating the QPD segments. We consider the five different configurations listed in Tab. III.

Figure 4 a) depicts the heterodyne efficiency under variation of the angle  $\alpha_{\text{rx}}$  while setting  $\beta_{\text{rx}} = 0$ . Hereby, values for beam parameters and the receiving optics have been taken from [25]. Note that in case of  $\beta_{\text{rx}} = 0$ , the heterodyne efficiency of all individual segments is equal so that only the results of segment 1 are plotted. All configurations have their maximum at  $\alpha_{\text{rx}} = 0$ . However, the heterodyne efficiency decreases much more rapidly with increased pointing error, i.e. increased  $\alpha_{\text{rx}}$ , for all four segments and the vertical segments than for segment 1 and the horizontal segments. In fact, it can be shown that  $\eta_{\text{het,all}}(\beta_{\text{rx}} = 0) = \eta_{\text{het,ver}}(\beta_{\text{rx}} = 0) \leq \eta_{\text{het,hor}}(\beta_{\text{rx}} = 0) = \eta_{\text{het,seg 1}}(\beta_{\text{rx}} = 0)$ , see appendix B.

The degradation in heterodyne efficiency can be explained with respect to phase differences that arise once light falls on the QPD under nonzero angles of incidence  $\alpha_{\text{rx}}$  and  $\beta_{\text{rx}}$ , as evident from Eq. 8. In this case, additional phase contributions arise that change along the area of integration, i.e. along the detector area. The graphical illustration of Fig. 5 a) shows that increasing angles lead to a dephasing of the coherent beam. The contribution of  $\alpha_{\text{rx}}$  in Eq. 8 leads to a dephasing along the  $y$ -axis. Thus, the heterodyne efficiency of two seg-

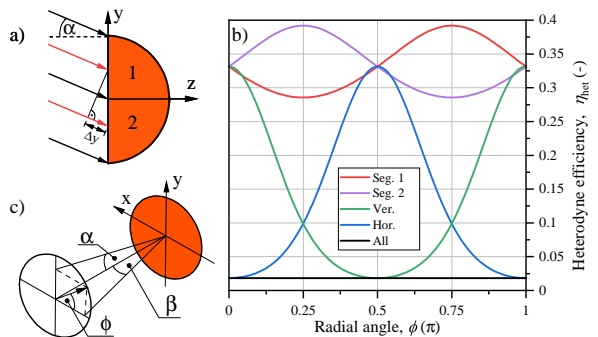


Figure 5. a) The effect of the signal beam hitting the QPD at a finite angle  $\alpha$  is illustrated. The local oscillator beam is omitted for clarity. The arrows colored red are used to indicate the resulting path-length difference  $\Delta y$ . b) The heterodyne efficiency for radial angle  $\phi$  with  $\gamma_{\text{max}} = M_2 \cdot 4.3 \mu\text{rad}$  is analyzed. Red and purple curves consider a readout of segment 1 and segment 2, respectively. The green curve combines segment 1 and segment 2, while the blue curve combines segment 1 and segment 4. The black curve combines all four segments of the QPD. c) Indication of radial angle  $\phi$  based on a unit circle separated by  $1/\tan(\gamma_{\text{max}})$  from the QPD.

ments combined along the  $x$ -axis (horizontal) surpasses the one of two segments combined along the  $y$ -axis (vertical), as no dephasing is present along the  $x$ -axis. Vice versa, if  $\beta_{\text{rx}}$  is varied while  $\alpha_{\text{rx}}$  is kept at zero, the heterodyne efficiency of two segments along the  $y$ -axis surpasses the one of two segments along the  $x$ -axis, as evident in Fig. 4 b). Finally, we note that for both scenarios combining all four segments always results in the lowest heterodyne efficiency, while a single segment leads to the maximum heterodyne efficiency.

Figure 5 b) depicts the heterodyne efficiency for a variation in  $\alpha_{\text{rx}}$  and  $\beta_{\text{rx}}$  expressed in terms of a combined radial angle  $\phi$ . Thereby, the angles are related as follows

$$\alpha_{\text{rx}} = \frac{1}{M_2} \text{atan}(\sin(\phi) \tan(\gamma_{\text{max}})),$$

$$\beta_{\text{rx}} = \frac{1}{M_2} \text{atan}(\cos(\phi) \tan(\gamma_{\text{max}})),$$

with a graphical illustration given in Fig. 5 c). Here, we introduced the parameter  $\gamma_{\text{max}}$  which defines the maximum angle of  $\alpha_{\text{rx}}$  and  $\beta_{\text{rx}}$ . For a maximum angle of  $\gamma_{\text{max}} = M_2 \cdot 4.3 \mu\text{rad}$ , we observe no variation in the heterodyne efficiency once all four segments are combined due to the rotational symmetry. The heterodyne efficiencies of two combined segments exhibit a periodicity of  $\pi$ . Maxima arise once the angle of incidence is normal to the alignment of the two QPD segments, in agreement to Fig. 4. The heterodyne efficiencies of single segments exhibit also a periodicity of  $\pi$ . Similar to the two segments, maxima of the single segments arise once the angle of incidence aligns with the maximum coherent integration path. For the single segments this path is along the lines tilted by  $\pm\pi/4$  to the  $x$  and  $y$ -axis.

For the given  $\gamma_{\text{max}}$ , the minimum heterodyne efficiency is

observed once all four segments are combined, while the maximum heterodyne efficiency is present at the single segments. However, at certain angles  $\phi$  the heterodyne efficiency of two combined segments surpasses the one of a single segment, which prevents a definite statement on the maximum heterodyne efficiency irrespective of  $\phi$ . A definite statement can be obtained when considering the maximum heterodyne efficiency of the single segments and their combinations. As shown in appendix B, the following inequality can be found that does not depend on  $\gamma_{\max}$  or  $\phi$

$$\max(\eta_{\text{het,seg 1}}, \eta_{\text{het,seg 2}}) \geq \max(\eta_{\text{het,hor}}, \eta_{\text{het,ver}}) \geq \eta_{\text{het,all}}. \quad (12)$$

The inequality in Eq. 12 is an important result in the ongoing discussion on the beat note acquisition process. In the following we will compare these three configurations regarding the maximum CNR.

#### D. Noise contributions

Dominant noise sources of the long-arm interferometer are shot noise, relative intensity noise (RIN) and electronic noise [25]. Stray light coupling noise is usually assumed to be very small and noise resulting from the pseudo-random noise modulation of the carrier, which is necessary to enable absolute ranging [15], can be adequately suppressed by suitable selection of the modulation scheme [17, 31]. In our investigations we adapt the model for RIN from [32]. To this, we consider only the  $1f$ -RIN contribution since this contribution exceeds the  $2f$ -RIN contributions in the context of LISA by more than two orders of magnitude [33]. Analytic models for shot noise and electronic noise are found in [29]. The three noise contributions are uncorrelated among each other and result in a total noise in  $V^2/\text{Hz}$  of

$$N_0(f) = \left( \frac{N_s N_{\text{QPD}} \eta_{\text{resp}}}{16} \right)^2 (P_{\text{lo}}^2 a_{\text{lo,1f}}^2 + P_s^2 a_{\text{s,1f}}^2) + 2e \frac{N_s N_{\text{QPD}} \eta_{\text{resp}}}{16} (P_{\text{lo}} + P_s) + s_{\text{I,seg,el}}^2 N_s N_{\text{QPD}} \quad (13)$$

The first line in Eq. 13 represents  $1f$ -RIN contribution, while the first and second term in the second line represent the shot and electronic noise contribution, respectively. Here,  $e$  denotes the electron charge,  $s_{\text{I,seg,el}}$  the electronic noise and  $a_{\text{1f}}$  the  $1f$ -RIN coupling [33]. Note that the factor of 16 in denominator of the  $1f$ -RIN contribution and the shot noise arises since the powers  $P_{\text{lo}}$  and  $P_s$  are defined per QPD. Both, shot noise and RIN, depend on the power of the local oscillator beam  $P_{\text{lo}}$  and the signal beam  $P_s$ . Since  $P_s/P_{\text{lo}} \lesssim 10^{-6}$  [33], noise contributions arising from  $P_s$  can be safely neglected in Eq. 13. Based on this approximation an expression for the

Table IV. Read-out configurations.

Configuration	CNR
One Segment	$\max(\text{CNR}_{\text{seg 1}}, \text{CNR}_{\text{seg 2}})$
Two segment	$\max(\text{CNR}_{\text{hor}}, \text{CNR}_{\text{ver}})$
Four segment	$\text{CNR}_{\text{all}}$

CNR following Eq. 10 and 13 can be formed

$$\text{CNR} \approx \frac{2\eta_{\text{carrier}}^2 \eta_{\text{resp}}^2 P_{\text{lo}} P_s (\alpha_{\text{tx}}, \beta_{\text{tx}}) \eta_{\text{wfe}} \eta_{\text{het}} (M_2 \alpha_{\text{rx}}, M_2 \beta_{\text{rx}})}{2e \frac{16\eta_{\text{resp}}}{N_s N_{\text{QPD}}} P_{\text{lo}} + (\eta_{\text{resp}} P_{\text{lo}} a_{\text{lo,1f}})^2 + \frac{16^2 s_{\text{I,seg,el}}^2}{N_s N_{\text{QPD}}}}. \quad (14)$$

Based on Eq. 14, only the heterodyne efficiency and the noise contributions from shot noise and electronic noise depend on the number of segments considered for the read-out. As shown in section II C, given  $\alpha_{\text{rx}} = \beta_{\text{rx}} = 0$  the heterodyne efficiency is independent of the segments and the number of segments considered for the read-out. In this case the CNR increases with increasing the number of segments  $N_s$ . However, if light is incident on the QPD at a nonzero angle, the highest heterodyne efficiency is found for  $N_s = 1$ , which in turn increases the CNR. These antagonistic effects are analyzed in the subsequent section.

#### E. Angle dependence of CNR

The CNR is a crucial parameter during the beat note acquisition process and details of the implications for the acquisition are discussed in the subsequent section. From Eq. 14 we found that the CNR depends in particular on the number of segments considered for the read-out, the received power and the heterodyne efficiency. The received power itself is a function of the angles  $\alpha_{\text{tx}}$  and  $\beta_{\text{tx}}$ , see Eq. 11, while the heterodyne efficiency depends on the angles  $\alpha_{\text{rx}}$  and  $\beta_{\text{rx}}$  and the QPD segments. The number of segments considered for the read-out is of particular interest. For a perfectly aligned signal beam, i.e.  $\alpha_{\text{rx}} = \beta_{\text{rx}} = 0$ , the CNR increases with increasing number of QPD segments. However, for nonzero incidence angles, i.e.  $\alpha_{\text{rx}} \neq 0$  and  $\beta_{\text{rx}} \neq 0$ , the heterodyne efficiency and thus the power of the beat note increases by reducing the number of segments, cf. Eq. 12. These antagonistic effects shall be analyzed in the following. Since the heterodyne efficiency explicitly depends on the number of the QPD segments, see Eq. 12, we put particular focus on the three configurations considered in Eq. 12. These three configurations will be denoted as one segment, two segment and four segment configuration. Thereby, the one segment configuration considers the maximum CNR of segment 1 and segment 2. The two segment configuration considers the maximum CNR

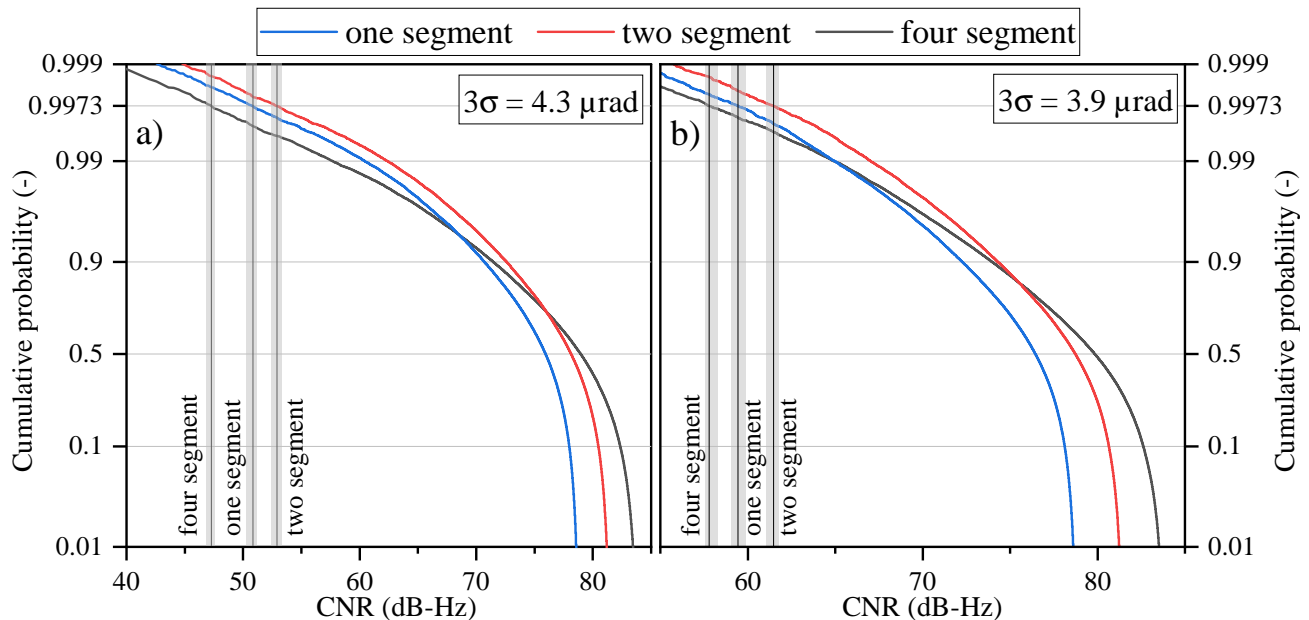


Figure 6. The CDF of the CNR for a variation of the angles  $\alpha_{tx}, \beta_{tx}, \alpha_{rx}$  and  $\beta_{rx}$  is depicted. Angles are drawn from a normal distribution with a  $3\sigma$  value of  $4.3 \mu\text{rad}$  and  $3.9 \mu\text{rad}$  in a) and b), respectively. Red and blue curves depict the CDF for the one and two segment configuration, respectively. The gray curves represent the CDF for the four segment configuration. Black vertical lines indicate the 0.997 value of the CDF. Labels at the bottom of the lines denote the respective configuration. In both figures the  $y$ -axis is scaled according to  $\ln(y/(1-y))$ .

of the vertical and horizontal combinations. Finally, the four segment configuration considers the CNR if the read-out of all four segments is combined, see also Tab. IV. Note that for the one and two segment configuration only two different read-outs are considered since the remaining read-outs are identical due to symmetry. The discussion on the implementation and implications of the maximum operation considered in the one and two segment configuration has been shifted to section III C.

The analysis is performed based on a Monte-Carlo simulation of Eq. 14 with  $1e5$  runs. Thereby, the angles  $\alpha_{tx}, \beta_{tx}, \alpha_{rx}$  and  $\beta_{rx}$  are drawn from a normal distribution with zero mean and variance  $\sigma$ . Their uncertainty ( $3\sigma$ ) is specified in Tab. II. Values of the beam characteristics and the transmitting and receiving optics have been taken from [25]. Finally, we note that the LISA long-arm interferometer consists of two QPD pairs operating in hot redundancy [34]. For the analysis we assume a separate processing of each QPD pair, while a combination of all QPDs is briefly discussed in section III C. Figure 6 depicts the cumulative probability function (CDF)  $F_{\text{CNR}}$  for the three configurations with respect to the CNR. Black vertical lines indicate the CNR value of  $F_{\text{CNR,lim}} := 0.997$ . This value of the CDF means that 99.7% of all simulations have a CNR that is equal or better than the value of the associated CNR. For the ongoing discussion this value will be used as the worst-case CNR. The  $1\sigma$  error of these vertical lines, which arises from the finite number of simulations, is indicated by gray boxes. In Fig. 6 a) the CDF is depicted for an angle uncer-

tainty of  $4.3 \mu\text{rad}$ . Here the two segment configuration exhibits the maximum  $F_{\text{CNR,lim}}$  at  $\sim 52.9$  dB-Hz. This value surpasses  $F_{\text{CNR,lim}}$  of the four segment configuration by roughly 5.6 dB.  $F_{\text{CNR,lim}}$  of the one segment configuration is around 2 dB smaller compared to the two segment configuration. Decreasing the angle uncertainty to  $3.9 \mu\text{rad}$  shifts  $F_{\text{CNR,lim}}$  by around 8.6 dB for the two segment configuration and very similar for the one segment configuration. For the four segment configuration this shift is even more prominent with a shift of 10.5 dB, which diminishes the distance between the two segment and four segment configuration to around 3.6 dB.

We can conclude that irrespective of the considered angle uncertainty ( $3.9 \mu\text{rad}$  or  $4.3 \mu\text{rad}$ ) the two segment configuration outperforms the one segment configuration and the four segment configuration based on the worst case CNR represented via  $F_{\text{CNR,lim}}$ .

### III. APPLICATION: FOURIER ACQUISITION

#### A. Fourier acquisition: basics and model assumptions

In the previous section we demonstrated that improved CNR levels of the beat note signal can be obtained through certain QPD read-out configurations. In the following we want to analyze the implications of the CNR levels on the LISA beat note acquisition scheme. The beat note acquisition of LISA relies on a Fourier



transform acquisition. The Fourier transform was also used for LISA Pathfinder even during nominal operation, where amplitude as well as phase information of a frequency bin were used to stabilize the laser frequency [35, 36]. However, for LISA this is not possible due to the much larger heterodyne frequency (several MHz instead of kHz for LISA Pathfinder) which changes dynamically due to orbit evolution and super-imposed frequency offsets [12].

The Fourier transform acquisition considered in the following has been detailed in [12, 18]. Upon reception, the beat note signal is digitized with a sampling rate of  $f_s = 80$  MHz. Then a fast Fourier transform (FFT) over  $L$  samples is used to convert the signal to the frequency domain, resulting in a frequency resolution of  $f_{\text{res}} = f_s/L$ . After taking the magnitude squared, a peak search algorithm selects the FFT bin with the maximum signal. It shall be noted that the peak search algorithm also incorporates the possibility to exclude certain bins from the search space. This is in particular useful in a laboratory environment to filter common reference frequencies, however, it will be omitted in the following.

The beat note must be within the receiver bandwidth ( $\approx 20$  MHz) and below the Nyquist frequency ( $f_s/2$ ) to allow a detection via the FFT acquisition. Since the frequency of the incident beam is in general not precisely known (uncertainty of around 100 MHz), the presence of the signal cannot be guaranteed for a Fourier transform acquisition over a single FFT interval. Consequently, the local oscillator beam performs a frequency scan over a predefined interval, in which presence of the beat note can be ensured. For each FFT interval, the peak search algorithm determines if the maximum of the current FFT interval supersedes the global maximum of all previous intervals. If this is the case the maximum of the current interval will be set as the new global maximum. Once the local oscillator has finished its scan pattern, the frequency bin associated with the global maximum is used as initial frequency for the PLL. In the end, the global maximum then represents the maximum of  $M$  number of FFT intervals. If each FFT interval contains  $K$  bins, then the global maximum represents the maximum over  $K_{\text{tot}} = K \cdot M$  frequency bins.

For the ongoing analysis we make the following assumptions

(1) Based on a suitable selection of the receiver front-end, we assume that frequencies above the Nyquist frequency are adequately suppressed [37] and aliasing will be neglected in the following.

(2) The finite sample number  $L$  per FFT leads to spectral leakage that may be suppressed via adequate window functions [38]. Once the beat note frequency does not correspond to the center frequency of a bin, a degradation of the signal bin power due to the spectral leakage is observed, while the power of adjacent bins is increased. This well-known behavior of the FFT is in particular addressed via interpolation algorithms [20, 39] and thus spectral leakage is omitted in the following. For a worst

case analysis, one may note that the effect is maximized once the beat note frequency is exactly in between the center frequencies of two bins. The resulting loss in power of the signal bin is known as scalloping loss, which is 3.92 dB for a rectangular window [40]. This worst case is briefly addressed in the subsequent section.

(3) The scan of the local oscillator beam in general ensures that the beat note is at least once present in one of the  $K_{\text{tot}}$  bins. It shall be noted that if presence cannot be ensured, threshold testing is usually performed to verify its presence. In turn, acquisition performance strongly depends on the threshold setting. To focus on the influence of the CNR on the acquisition performance, presence of the main beat note will be assumed in the following.

Moreover, as the scan pattern of the local oscillator beam is not defined yet and based on assumption (2), we assume that the signal is present in only one of the  $K_{\text{tot}}$  bins. This would either correspond to a step-scan pattern with non-overlapping FFT intervals or to a linear scan pattern at a known scan rate. In case of the latter, effects resulting from the linearly changing frequency can be adequately compensated by taking into account the discrete chirp-Fourier transform [41]. In this way the acquisition can also be regarded as a single acquisition for  $K_{\text{tot}}$  bins.

(4) Besides the phase information, the beat note of LISA also enables the transmission of auxiliary functions, in particular PRN sequences to enable pseudo-range measurements, data transfer and clock jitter transfer [16, 31, 42]. Similar concepts are also proposed for the TianQin mission [43–45]. All of these auxiliary functions are realized via low-depth phase modulations of the carrier, resulting in loss of power for the science signal, which has been accounted for in Eq. 10 by the factor  $\eta_{\text{carrier}}$ . Around 10% of the power is used for the generation of optical sidebands incorporating the clock jitter. Upon interference with the local oscillator beam, these optical sidebands form sideband/sideband beat notes one megahertz apart from the main beat note and well above the noise floor [12, 46, 47]. Consequently, these sideband/sideband beat notes might lead to false detection and need to be adequately addressed in the following. PRN sequences and data transmission are realized via a chip modulation, which consists only of 1% of the carrier power. Depending on the chip modulation, the maxima are either in close vicinity to the main beat note or the sideband/sideband beat notes with noise density maxima of the order of the shot noise. This and the fact that the chip modulation can easily be suppressed, e.g., by transmitting a PRN code of constant zeros, allows us to omit this additional noise contribution in the following.

## B. Probability of detection

Based on the assumptions (1) to (4), the influence of the CNR on the performance of the beat note acquisi-

tion scheme can be studied in an analytical framework delineated in the following. Acquisition performance is usually evaluated in terms of the PD and the probability of false alarm. To focus analysis on the CNR, we assumed presence of the main beat note in one of the bins, see assumption (3), which makes PD and probability of false alarm  $P_{fa}$  exclusive, i.e.  $1 = P_{fa} + P_D$ . Consequently, for the ongoing analysis we focus on the PD, while the probability of false alarm can be directly retrieved from these results.

For the definition of a correct detection and thus for the evaluation of the PD, understanding the operating principle of the acquisition scheme within the phasemeter is crucial: Due to the finite frequency resolution of the FFT, the output of the beat note acquisition does not necessarily correspond to the exact beat note frequency. Instead it represents the initial value for the numerically controlled oscillator (NCO) of the PLL. A second-order Type 2 PLL, as it is the case for LISA [12], is then in general capable to achieve the lock. Hereby, the time to lock depends on the loop parameters, in particular on the loop bandwidth, and the frequency offset between the beat note and the initial frequency of the NCO [48]. Consequently, alignment between the frequency resolution of the FFT and the PLL loop parameters is generally required and will be assumed in the ongoing analysis. To this end, we do not take into account spectral leakage as elaborated in section III A, assumption (2). This simplification is especially important as spectral leakage increases only the noise bins in close vicinity of the beat note. Consequently, only these bins will be more likely to be selected in case of spectral leakage. However, based on the phasemeter design, a selection of such a noise bin does not result in an entirely false detection but may only increase the final time to lock of the PLL.

Based on the assumptions listed in section III A, the signal present at the FFT consists of the main beat note, sideband/sideband beat notes and additive noise. The additive noise is modeled as Gaussian noise with one-sided noise power density  $N_0$  as given in Eq. 13. The power of the sinusoidal beat note is stated in Eq. 10. Expressions on the power of the sideband/sideband beat notes have been obtained from [29]. In this sense, the input signal represents a real-valued Gaussian random process. We note that real and imaginary part of each FFT bin again represent a Gaussian process [49]. For an FFT that is normalized to its sample size, the variance of real and imaginary part is given by  $\sigma_{bin}^2 = \frac{N_0 f_{res}}{4}$ , irrespective if the bin contains the beat note and noise, or only noise. Real and imaginary parts are then combined in a random variable  $S_{bin}$  using the magnitude squared operation. As shown in [50, 51], the probability density function (PDF) of the normalized variable  $s = S_{bin}/\sigma_{bin}^2$  for bin  $k$  follows

$$f_k(s) = \frac{1}{2} e^{-\frac{s+\delta_k}{2}} I_0(\sqrt{s\delta_k}), \quad (15)$$

where  $I_0$  denotes the zero order modified Bessel function and  $\delta$  the non-centrality parameter. Noise bins are un-

biased and follow a central  $\mathcal{X}_2^2$ -distribution, i.e.  $\delta_k = 0$ . The bins containing the main beat note and the sideband/sideband beat note are drawn from a non-central  $\mathcal{X}_2^2$ -distribution with non-centrality parameter

$$\delta_{main} = \frac{2CNR}{f_{res}} \quad (16)$$

and

$$\delta_{sb} = \frac{J_1^2(m_{sb})}{\eta_{carrier}^2} \delta_{main}, \quad (17)$$

respectively. Hereby, the first order Bessel function  $J_1$  is a result of the low-depth phase modulation with modulation index  $m_{sb}$  for the side-bands. The modulation index will be assigned with  $m_{sb} = 0.45$ , which results in total power of about 10% for the sideband/sideband beat notes (5% per sideband/sideband beat note) [29].

Based on the PDF of signal and noise bins, it is now possible to define the PD. A correct detection is achieved when the power of the bin containing the main beat note exceeds all remaining ones. Without loss of generality, we set bin  $j$  as the signal bin, i.e.  $\delta_j = \delta_{main}$ . The analytical formulation of the PD is given by the analysis of [52]

$$P_D = \int_0^\infty f_j(s) \prod_{\substack{k=0 \\ k \neq j}}^{K_{tot}-1} F_k(s) ds, \quad (18)$$

where  $F_k(s)$  denotes the CDF of bin  $k$ . The CDF can be directly retrieved via integration of Eq. 15. In fact, the product series contains only two types of CDF, namely the CDF for the noise bins and the CDF for the sideband/sideband beat notes. We then find

$$P_D = \int_0^\infty \frac{1}{2} e^{-\frac{s+\frac{2CNR}{f_{res}}}{2}} I_0(\sqrt{s\frac{2CNR}{f_{res}}}) \cdot [1 - e^{-\frac{s}{2}}]^{K_{tot}-3} [1 - Q_1(\sqrt{\delta_{sb}}, \sqrt{s})]^2 ds, \quad (19)$$

where the first line is the contribution from the main beat note and the second line the contribution from all other bins. The function  $Q_1$  denotes the Marcum  $Q$ -function of order one [53].

To examine the influence of the sideband/sideband beat notes on the PD, we will also consider the PD in the case when – besides the main beat note – there are only noise bins, denoted as  $P_{D,n}$ . In this case the PD reads as

$$P_{D,n} = \int_0^\infty \frac{1}{2} e^{-\frac{s+\frac{2CNR}{f_{res}}}{2}} I_0(\sqrt{s\frac{2CNR}{f_{res}}}) [1 - e^{-\frac{s}{2}}]^{K_{tot}-1} ds. \quad (20)$$

In fact, following [54] Eq. 20 can be approximated for high PD values as

$$P_{D,n} \approx 1 - (K_{tot} - 1) \frac{e^{-\frac{CNR}{2f_{res}}}}{2}. \quad (21)$$

The ongoing analysis is based on the analytical expression of Eq. 18 to Eq. 21, however, numerical simulations

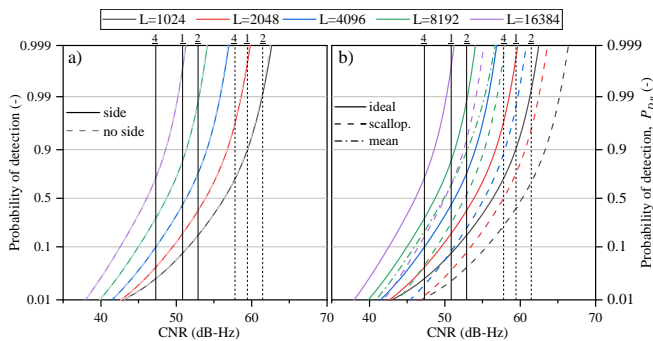


Figure 7. The PD is plotted over the CNR for different FFT lengths  $L$ . In addition, in a) the PD for a signal including (solid lines) and excluding (dashed lines) sideband/sideband beat notes is depicted. In b) the effect of scalloping loss is considered (dashed lines) compared to the case, where the frequency is located at the bin center (solid lines). Moreover for a FFT length of  $L = 8192$  also the mean loss due to spectral leakage is depicted (dashed-dotted line). In both figures the CNR values for an angle uncertainty of  $3.9 \mu\text{rad}$  (dashed lines) and  $4.3 \mu\text{rad}$  (solid lines) at  $F_{\text{CNR,lim}}$  for the one segment (1), two segment (2) and four segment (4) configuration are indicated by black vertical lines with respective underlined numbers at the top of each line. In both figures the  $y$ -axis is scaled according to  $\ln(y/(1-y))$ .

have been conducted to justify these results.

First we want to study the influence of the sideband/sideband beat notes on the PD. Figure 7 a) depicts the PD in presence (Eq. 19) and absence (Eq. 20) of sideband/sideband beat notes by solid and light-dashed lines, respectively. The lines match near perfectly, revealing that for the given modulation index the influence of the sideband/sideband beat notes on the PD is negligible. For the ongoing analysis we will, therefore, restrict us to the case where sideband/sideband beat notes are absent. Moreover, this result also shows that the benefit in suppressing the optical sideband modulation during the beat note acquisition is rather small from the point of false detection and is mainly due to the increase of power in the main beat note ( $\eta_{\text{carrier}} \rightarrow 1$ ).

In addition, Fig. 7 a) depicts the PD for different frequency resolutions. Variation of the frequency resolution  $f_{\text{res}}$  is thereby expressed via a variation of the FFT length  $L$ . This emphasizes the fact, that in a practical application, sampling rate and spectrum of interest are fixed. Values of  $L$  are based on previous analysis [12, 18, 24] and the fact that  $L$  being an integer power of 2 enables an implementation via standardized and simple FFT algorithms [18]. Finally, it must be noted that laser frequency noise leads to a broadening of the laser line width [55], which in turn broadens the main beat note. Therefore, the frequency resolution and consequently the FFT length  $L$  must be chosen such that the substantial part of the main beat note power falls inside a single frequency bin of the FFT. Although for LISA-representative lasers this should generally still be ensured with an FFT

length of  $L = 16384$ , previous studies focused on smaller FFT lengths. Therefore, we will particularly focus on  $L = 8192$ , which we will assume as baseline in the following.

Importantly, an increase in the FFT length  $L$  – besides the improved frequency resolution  $f_{\text{res}}$  – also leads to an increasing number of noise bins  $K_{\text{tot}} - 1$ . In turn, an increasing number of noise bins decreases the PD, as apparent from Eq. 21. Consequently, although the contribution of the frequency resolution  $f_{\text{res}}$  and the CNR on the PD are theoretically equal, as apparent from Eq. 20, in a practical application this is not the case and the PD is most sensitive to the CNR. This can also be observed in Fig. 7 a), which depicts the PD for a single FFT interval covering a spectrum of 20 MHz. Frequency resolution of the purple curve is increased by a factor of 16 compared to the gray curve. This would correspond to a shift of 12 dB between both curves. However, the actual shift at high values is only around 11.4 dB due to the influence of the increased number of noise bins.

In Fig. 7 b) the effect of scalloping loss for a rectangular window is illustrated. Irrespective of the FFT length, it leads to a shift of the curves by value of the scalloping loss (3.92 dB), which is a direct consequence from Eq. 20. In addition, for a FFT length of  $L = 8192$ , also the PD considering the mean power loss due to spectral leakage has been taken into account. Based on the operating principle of the acquisition scheme within the phasemeter, spectral leakage has been incorporated in Eq. 20 via a decrease in CNR in the signal bin. The resulting PD is shifted by around 1 dB from the ideal PD line, i.e. when the frequency is located at the bin center, for PD values of  $\approx 0.5$ . Towards higher PD values the influence of the spectral leakage increases to around 2.6 dB at  $\text{PD} = 0.999$ .

PD curves are brought into perspective with the different read-out schemes discussed in section II E via the black vertical lines indicating the value of  $F_{\text{CNR,lim}}$  for an angle uncertainty of  $3.9 \mu\text{rad}$  (dashed lines) and  $4.3 \mu\text{rad}$  (solid lines). In case of an angle uncertainty of  $4.3 \mu\text{rad}$ , only the one and two segment configuration with an FFT length of  $L = 16384$  achieve a high PD ( $> 99\%$ ). For  $3.9 \mu\text{rad}$  the two segment configuration guarantees a high PD over all FFT lengths considered in the analysis if the beat note frequency is located at the bin center, while the four segment configuration requires an FFT length of  $L \geq 4096$ . Once the signal is located in between two bins, a high PD cannot be guaranteed for an angle uncertainty of  $4.3 \mu\text{rad}$  irrespective of the configuration, while for an angle uncertainty of  $3.9 \mu\text{rad}$  a high PD is obtained at an FFT length of  $L \geq 4096$  and  $L \geq 8192$  for the two and four segment configuration, respectively.

The majority of these results retains its validity once multiple FFT intervals are considered. As depicted in Fig. 8 a), at high PD values the influence of an increasing number of FFT intervals  $M$  is rather small, yielding a CNR shift of around 0.5 dB for  $M = 5$  at  $\text{PD}_{\text{n}} = 0.99$ . An increasing influence is observed towards lower PD values.

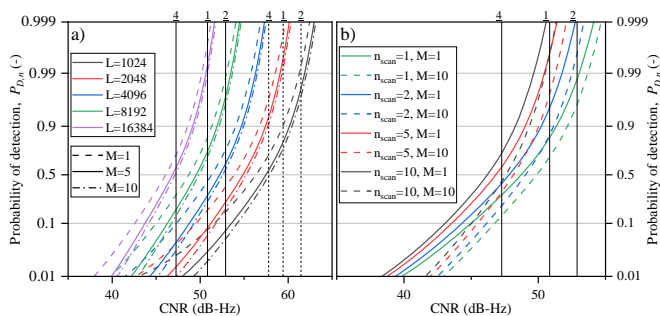


Figure 8. The influence of multiple FFT intervals on the PD is analyzed in a). Dashed lines depict the PD for a single interval, while solid and dashed-dotted lines show the resulting PD for five and ten FFT intervals, respectively. In b) the influence of multiple scans is analyzed. The PD for a single scan is depicted by the green plots. The PD for two, five and ten scans is depicted by the blue, red and gray lines, respectively. Solid lines represent the PD for a single FFT interval, while dashed lines show the PD for ten FFT intervals. CNR values for an angle uncertainty of  $3.9 \mu\text{rad}$  (dashed lines) and  $4.3 \mu\text{rad}$  (solid lines) at  $F_{\text{CNR,lim}}$  for the one segment (1), two segment (2) and four segment (4) configuration are indicated by black vertical lines with respective underlined numbers at the top of each line. In both figures the  $y$ -axis is scaled according to  $\ln(y/(1-y))$ .

As a baseline case we may consider a receiver bandwidth of 20 MHz and an uncertainty of laser frequency of 100 MHz, necessitating a laser frequency scan over approximately 5 FFT intervals. In this case for an angle uncertainty of  $4.3 \mu\text{rad}$  and an FFT length of  $L = 8192$ , the PD of the two segment configuration is around 0.97, while the PD of the four segment configuration is only at around 0.17. This result clearly highlights the performance improvement obtained through the two segment configuration. However, even the PD of the two segment configuration may not be suitable and a greater FFT length might be required.

Another method to increase the PD is to perform multiple scans over the spectrum of interest. It shall be noted that variations of the main beat note due to the relative SC motion does not affect this method. The relative velocity of the SC is around 15 m/s [56]. This leads to slowly varying Doppler shifts negligible on the time scale of the FFT acquisition. Consequently, the signal will remain in the same bin for each scan. Combining the scans, there will be  $n_{\text{scan}}K_{\text{tot}}$  bins and the main beat note will be contained in  $n_{\text{scan}}$  bins, where  $n_{\text{scan}}$  equals the number of scans. Again selecting the main beat note based on the maximum bin power, the PD in absence of the sideband/sideband beat notes can still be calculated via Eq. 20 with the following adaptations: The PDF of the main beat note needs to be replaced with the maximum PDF of  $n_{\text{scan}}$  beat notes, which is given by  $n_{\text{scan}}f_j(s)(1 - Q_1(\sqrt{\delta_{\text{main}}}, \sqrt{s}))^{n_{\text{scan}}-1}$ . In the same way also the number of noise bins increases to  $n_{\text{scan}}(K_{\text{tot}} - 1)$ . Figure 8 b) depicts the resulting PD for a fixed FFT

length of  $L = 8192$ . An increase in  $n_{\text{scan}}$  results in an increased PD. The performance increase from one to five signal bins is thereby comparable with switching from the read-out scheme of the one segment configuration to the two segment configuration for an angle uncertainty of  $4.3 \mu\text{rad}$ . Importantly, the influence of multiple scans is most relevant at high PD values. Already two scans can ensure  $P_{D,n} > 0.99$  for the two segment configuration for an FFT interval of  $M = 10$ , an FFT length of  $L = 8192$ , and an angle uncertainty of  $4.3 \mu\text{rad}$ . However, multiple scans result in an increased acquisition time.

In summary, analysis of the PD revealed that the CNR values, where the CDF reaches 99.7% for an angle uncertainty of  $3.9 \mu\text{rad}$  and  $4.3 \mu\text{rad}$ , are in a critical region, where depending on the FFT acquisition parameters, high PD values ( $> 0.99$ ) cannot be ensured. Increasing the FFT length  $L$  or the number of scans over the spectrum of interest can increase the PD. This, however, comes at the price of higher processing load and an increased processing time. Moreover, it has been shown that the PD is most sensitive to the CNR compared to aforementioned FFT acquisition parameters. In consequence, in particular for an angle uncertainty of  $4.3 \mu\text{rad}$ , the increase in CNR provided by the two segment configuration led to a strong PD improvement compared to the four segment configuration. Irrespective of the angle uncertainty, these results highlight the advantages and necessity of a well-considered decision on the read-out scheme.

In addition, the analysis revealed the importance of reducing the errors in the angle uncertainty. The shift in the uncertainty budget for  $3.9 \mu\text{rad}$  instead of  $4.3 \mu\text{rad}$ , already shifts the black vertical lines to the right by about 9 dB. This statement highlights the large payoff to be gained by slightly reducing the various errors that enter the uncertainty budget.

### C. Discussion

For the considered angle uncertainties of  $3.9 \mu\text{rad}$  and  $4.3 \mu\text{rad}$ , the two segment configuration outperforms the one and four segment configurations in terms of CNR. The previous section highlighted the importance of the CNR, and consequently also the adequate selection of the read-out configurations, on the FFT acquisition. In the following, the implementation of the read-out configurations in terms of the FFT acquisition shall be addressed. One and two segment configuration rely on the maximum operation as defined in section II E. In terms of the FFT acquisition, the implementation of the maximum operation of two different read-outs necessitates two separate FFT acquisition schemes, where at the end the maximum of both acquisition schemes is considered. Taking into account the assumptions made in section III A, the expectation of the output then equals the maximum CNR of both read-outs.

Since the maximum operation and thus a second FFT is

only considered for the one and two segment configuration, naturally the question arises about a second FFT (1) or and increased frequency resolution (2) for the four segment configuration. This shall be briefly discussed in the following:

(1) A second FFT could be used to consider the read-out of additional QPDs operating in hot redundancy. Hereby, the output of both could be used to form a maximum operation as it is done for the one and two segment configuration. Since the CNR is equal for both read-outs the PD is described by Fig. 8 b) for  $n_{\text{scan}} = 2$ . The curve for  $n_{\text{scan}} = 2$  is shifted by around 1 to 2 dB compared to  $n_{\text{scan}} = 1$ . This is well below the CNR increase of the two segment configuration compared to the four segment (3.7 dB for an angle uncertainty of  $3.9 \mu\text{rad}$  and 5.6 dB for  $4.3 \mu\text{rad}$ ).

In fact, the second output could also be used to form a summation of both FFTs after taking the magnitude squared. The PD is then obtained via Eq. 18 by noting that the bin power follows a  $\chi_4^2$ -distribution with non-centrality parameter  $2\delta$ . This type of summation corresponds to an incoherent summation and has been detailed [24].

(2) It is well-known that the operations of a FFT scale with  $\mathcal{O}(L \log L)$  [57]. Consequently for large  $L$ , instead of a second FFT, a FFT with roughly double the frequency resolution could be used. Based on the findings in section IIIB this would shift the PD curve by  $<3\text{dB}$ .

Consequently, irrespective of the angle uncertainty ( $3.9 \mu\text{rad}$  or  $4.3 \mu\text{rad}$ ) the two segment configuration would still outperform the four segment configuration.

#### IV. CONCLUSION

In this paper we analyzed the coherent acquisition architecture for LISA, determining the feasibility range and optimizing the driving design parameters. Two major aspects are highlighted: the CNR of the beat note signal read from the QPD for different read-out configurations, and the probability of detection for the baseline acquisition scheme with focus on the CNR.

The CNR is governed by the power of the received beam, the heterodyne efficiency of the interference signal, and the noise affecting the signal and its phase readout. These quantities depend on the angles of the transmitted beam and of the received beam with respect to the line-of-sight in between two SC, where the residual pointing errors are incurred from the preceding spatial acquisition phase. The heterodyne efficiency plays a special role as it is the only quantity that depends on the coherence between local and received beam. Detailed analysis on the heterodyne efficiency revealed that single segments of a QPD are less sensitive to a pointing error compared to two combined segments. In particular, it could be shown that the maximum heterodyne efficiency of two adjacent single segments (one segment configuration) always outperforms the maximum CNR of any combina-

tion of two adjacent segments (two segment configuration). The heterodyne efficiency once all four segments of a QPD are combined (four segment configuration) is in any case most sensitive to pointing errors.

Considering this effect, and also the dependency of the received beam power on the angle of the transmitted beam, we find from Monte Carlo simulations that the expected minimum CNR of the beat note signal is highest for the two segment configuration. In this configuration and for  $4.3 \mu\text{rad}$  pointing error ( $3\sigma$ ), the expected minimum CNR exceeds the four segment configuration by 5.6 dB. The minimum CNR for all configurations was defined from the respective cumulative probability at the 99.73% level, meaning that 99.73% of simulations yield better or equal CNR.

Application and influence of the configurations on the beat note acquisition has been analyzed in the second part of the paper. The minimum CNR is the most essential parameter for calculating the probability of detecting the beat note for which an FFT peak search algorithm is baselined for LISA. The PD is also strongly impacted by the number of points used in the FFT, i.e., the measurement time, as well as the spectral leakage, which is analyzed in terms of the scalloping loss, while false detection due to the optical sidebands are found to have only negligible effect. Furthermore, we considered the impact of the number of frequency search intervals on the PD, noting that the uncertainty of laser frequency ( $\approx 100 \text{ MHz}$ ) is much higher than the phasemeter bandwidth ( $\approx 20 \text{ MHz}$ ). Taking all these effects into account and assuming the minimum CNR found for each configuration, we find that for the two segment configuration the PD is around 97% while for the four segment configuration it is only around 17%. Here, we assumed an angular uncertainty of  $4.3 \mu\text{rad}$  and 8192 FFT points, while scalloping loss has been neglected. We also showed the possibility of increasing the PD by performing multiple scans across the same frequency range, but this comes at the expense of longer measurement times.

Finally, analyses have been extended taking into account that the implementation of the one and two segment configurations necessitates a second FFT acquisition scheme. It was shown that when considering similar additions for the four segment configuration, e.g. by doubling the FFT length, the two segment configuration still outperforms the four segment configuration in terms of minimum CNR.

The analysis approach and models presented in this paper may be used as the framework for defining the architecture and design parameters of the coherent acquisition phase for LISA or other interferometry missions in space.

#### ACKNOWLEDGMENTS

The authors thank T. Ziegler, O. Mandel, S. Delchambre, P. Gath and P. Voigt for their support and fruitful discussions.

This work was supported by funding from the Max-Planck-Institut für Gravitationsphysik (Albert-Einstein-Institut), based on a grant by the Deutsches Zentrum für Luft- und Raumfahrt (DLR). The work was supported by the Bundesministerium für Wirtschaft und Klimaschutz based on a resolution of the German Bundestag (Project Ref. Number 50 OQ 1801).

## Appendix A: Heterodyne efficiency

In the following, we derive an expression for the heterodyne efficiency  $\eta_{\text{het}}$  for a single segment, two combined segments and four combined segments of a QPD. Following the definition in Eq. 6, the heterodyne efficiency in the ORF is given by

$$\begin{aligned} \eta_{\text{het}} &= \frac{\left| \iint E_s^*(\alpha_{\text{tx}}, \beta_{\text{tx}}, \alpha_{\text{rx}}, \beta_{\text{rx}}) E_{\text{lo}} dS \right|^2}{\iint |E_s|^2 dS \iint |E_{\text{lo}}|^2 dS} \\ &= \frac{(\frac{1}{2}c\epsilon_0)^2 |E_s^0(\alpha_{\text{tx}}, \beta_{\text{tx}})|^2 |E_{\text{lo}}^0|^2}{(N_s/4)^2 P_s P_{\text{lo}}} \left| \iint \exp(ik_s(x \sin(M_2\beta_{\text{rx}}) - y \sin(M_2\alpha_{\text{rx}}) \cos(M_2\beta_{\text{rx}}))) \exp\left(-\frac{x^2 + y^2}{W_0^2}\right) d\tilde{S} \right|^2 \\ &= \frac{c\epsilon_0 |E_{\text{lo}}^0|^2}{2\pi(N_s/4)^2 R_{\text{min}}^2 P_{\text{lo}}} \left| \iint \exp(-(x^2/W_0^2 - ik_s x \sin(M_2\beta_{\text{rx}}))) \exp(-(y^2/W_0^2 + ik_s y \sin(M_2\alpha_{\text{rx}}) \cos(M_2\beta_{\text{rx}}))) d\tilde{S} \right|^2. \end{aligned} \quad (\text{A1})$$

Hereby,  $d\tilde{S}$  indicates that, in contrast to  $dS$ , integration is only performed over the area that is not clipped by the aperture with radius  $R_{\text{min}}$  (see section II A). We note that the power of the local oscillator beam (Eq. 2) at the QPD is given by:

$$P_{\text{lo}} = \frac{1}{2}c\epsilon_0 \iint_{\text{all}} |E_{\text{lo}}|^2 dS = \frac{1}{2}c\epsilon_0 \int_0^{R_{\text{QPD}}} \int_0^{2\pi} |E_{\text{lo}}^0|^2 \cdot e^{-2(r/W_0)^2} r d\varphi dr = \pi c\epsilon_0 |E_{\text{lo}}^0|^2 \frac{W_0^2}{4} \left[ 1 - e^{-2(R_{\text{QPD}}/W_0)^2} \right].$$

Consequently, the amplitude reads as

$$E_{\text{lo}}^0 = \frac{1}{W_0 \sqrt{2\pi c\epsilon_0}} \sqrt{P_{\text{lo}}} N(R_{\text{QPD}}/W_0), \quad \text{with } N(x) := 2^{3/2} \left( 1 - e^{-2x^2} \right)^{-1/2}. \quad (\text{A2})$$

Inserting Eq. A2 in Eq. A1 yields

$$\eta_{\text{het}} = \left( \frac{2N(R_{\text{QPD}}/W_0)}{N_s W_0 \pi R_{\text{min}}} \right)^2 \left| \iint \exp(-(x^2/W_0^2 - ik_s x \sin(M_2\beta_{\text{rx}}))) \exp(-(y^2/W_0^2 + ik_s y \sin(M_2\alpha_{\text{rx}}) \cos(M_2\beta_{\text{rx}}))) d\tilde{S} \right|^2. \quad (\text{A3})$$

Finally, expanding the term in the first exponential function according to

$$\begin{aligned} \eta_{\text{het}} &= \left( \frac{2N(R_{\text{QPD}}/W_0)}{N_s W_0 \pi R_{\text{min}}} \right)^2 \exp\left(-\frac{1}{2}W_0^2 k_s^2 \sin^2(M_2\beta_{\text{rx}})\right) \cdot \\ &\quad \cdot \left| \iint \exp\left(-\left(x/W_0 - \frac{i}{2}W_0 k_s \sin(M_2\beta_{\text{rx}})\right)^2\right) \exp(-y^2/W_0^2 - ik_s y \sin(M_2\alpha_{\text{rx}}) \cos(M_2\beta_{\text{rx}})) d\tilde{S} \right|^2 \end{aligned}$$

enables the integration in Cartesian coordinates i.e.  $d\tilde{S} \rightarrow dx dy$ . Therefore, we introduce the following notation

$$\text{erf}(a, b) := \text{erf}(a) - \text{erf}(b), \quad \text{with } \text{erf}(x) = \frac{2}{\sqrt{\pi}} \int_0^x e^{-t^2} dt, \quad (\text{A4})$$

which results in

$$\begin{aligned} \eta_{\text{het}} &= \left( \frac{N(R_{\text{QPD}}/W_0)}{N_s \sqrt{\pi} R_{\text{min}}} \right)^2 \exp\left(-\frac{1}{2}W_0^2 k_s^2 \sin^2(M_2\beta_{\text{rx}})\right) \cdot \\ &\quad \cdot \left| \int_{y^-}^{y^+} \text{erf}\left(\frac{x^+}{W_0} - \frac{i}{2}W_0 k_s \sin(M_2\beta_{\text{rx}}), \frac{x^-}{W_0} - \frac{i}{2}W_0 k_s \sin(M_2\beta_{\text{rx}})\right) \exp(-y^2/W_0^2 - ik_s y \sin(M_2\alpha_{\text{rx}}) \cos(M_2\beta_{\text{rx}})) dy \right|^2. \end{aligned} \quad (\text{A5})$$

Hereby, selection of  $y^\pm$  and  $x^\pm$  according to Tab. III enables to calculate the heterodyne efficiency  $\eta_{\text{het}}$  for a single segment, two combined segments and all four combined segments of a QPD.

## Appendix B: Angle dependence of heterodyne efficiency

In this appendix we evaluate the heterodyne efficiency for various segments when the signal beam hits the QPD

at a certain angle of incidence. To this end, we will adopt

the notation specified in Tab. III. The evaluation will be performed based on Eq. A5. However, to reduce the amount of lengthy expressions, we will focus only on the terms which differ among the segments and segment con-

figurations, and denote this parameter as  $\eta'_{\text{het}}$ . Clearly, the results also hold for  $\eta_{\text{het}}$ . Based on Eq. A5, we will define  $\eta'_{\text{het}}$  as

$$\eta'_{\text{het}} := \frac{1}{N_s^2} \left| \int_{y^-}^{y^+} \operatorname{erf} \left( \frac{x^+}{W_0} - \frac{1}{2} i W_0 k_s \sin(M_2 \beta_{\text{rx}}), \frac{x^-}{W_0} - \frac{1}{2} i W_0 k_s \sin(M_2 \beta_{\text{rx}}) \right) \exp(-y^2/W_0^2 - i k_s y \sin(M_2 \alpha_{\text{rx}}) \cos(M_2 \beta_{\text{rx}})) dy \right|^2. \quad (\text{B1})$$

Moreover, the following identities of definition A4 will be particularly useful

$$\operatorname{erf}(a + bi, -a + bi) \in \mathbb{R} \quad (\text{B2})$$

$$\Re\{\operatorname{erf}(a + bi, bi)\} = \frac{1}{2} \operatorname{erf}(a + bi, -a + bi) \quad (\text{B3})$$

$$(\operatorname{erf}(a + bi, bi))^* = \operatorname{erf}(bi, -a + bi) \quad (\text{B4})$$

$$\operatorname{erf}(a, -a) = 2 \operatorname{erf}(a) \quad (\text{B5})$$

with  $a, b \in \mathbb{R}$ . Proofs for the identities are straightforward by expressing the complex error function in definition A4 through line segments as done in [58].

First we will consider a variation of the angle of incidence only along one axis and set  $\beta_{\text{rx}} = 0$ . Starting with two combined segments ( $N_s = 2$ ) along the horizontal axis we have  $x^+ = -x^-$ . Therefore, taking into account Eq. B5,  $\eta'_{\text{het}}$  as defined in Eq. B1 yields

$$\eta'_{\text{het,hor}} = \left| \int_0^{R_{\text{min}}} \operatorname{erf} \left( \frac{\sqrt{R_{\text{min}}^2 - y^2}}{W_0} \right) \exp(-y^2/W_0^2) \exp(-i k_s y \sin(M_2 \alpha_{\text{rx}}) \cos(M_2 \beta_{\text{rx}})) dy \right|^2. \quad (\text{B6})$$

On the other hand for the vertical segments (segments 1+2) in case of  $\beta_{\text{rx}} = 0$  we have

$$\eta'_{\text{het,ver}} = \frac{1}{4} \left| \int_{-R_{\text{min}}}^{R_{\text{min}}} \operatorname{erf} \left( \frac{\sqrt{R_{\text{min}}^2 - y^2}}{W_0} \right) \exp(-y^2/W_0^2) \exp(-i k_s y \sin(M_2 \alpha_{\text{rx}}) \cos(M_2 \beta_{\text{rx}})) dy \right|^2 \quad (\text{B7})$$

$$= \left| \int_0^{R_{\text{min}}} \operatorname{erf} \left( \frac{\sqrt{R_{\text{min}}^2 - y^2}}{W_0} \right) \exp(-y^2/W_0^2) \cos(k_s y \sin(M_2 \alpha_{\text{rx}}) \cos(M_2 \beta_{\text{rx}})) dy \right|^2. \quad (\text{B8})$$

In the last line we applied Euler's formula and noted that the only odd function in B7 is the sine. From Eq. B6 and Eq. B8 it is now clear that:  $\eta'_{\text{het,ver}}(\beta_{\text{rx}} = 0) \leq \eta'_{\text{het,hor}}(\beta_{\text{rx}} = 0)$  and equivalently  $\eta_{\text{het,ver}}(\beta_{\text{rx}} = 0) \leq \eta_{\text{het,hor}}(\beta_{\text{rx}} = 0)$ . Moreover, in a similar way it can be shown that  $\eta_{\text{het,ver}}(\alpha_{\text{rx}} = 0) \geq \eta_{\text{het,hor}}(\alpha_{\text{rx}} = 0)$ . We also note that in case of  $\beta_{\text{rx}} = 0$  a single segment results in the identical heterodyne efficiency as  $\eta_{\text{het,hor}}$ , while combining all four segments leads to the heterodyne efficiency of  $\eta_{\text{het,ver}}$ . Consequently, we have  $\eta_{\text{het,seg } j}(\alpha_{\text{rx}} = 0) \geq \eta_{\text{het,all}}(\alpha_{\text{rx}} = 0)$  and  $\eta_{\text{het,seg } j}(\beta_{\text{rx}} = 0) \geq \eta_{\text{het,all}}(\beta_{\text{rx}} = 0)$  with  $j \in \{1, 2\}$ .

In the following, we will examine the heterodyne efficiency under variation of  $\alpha_{\text{rx}}$  and  $\beta_{\text{rx}}$ . At first we analyze  $\eta'_{\text{het}}$  for two combined segments ( $N_s = 2$ ) compared to four combined segments ( $N_s = 4$ ). For the two segments we will consider the horizontal segments, however, the procedure can easily be transferred to the vertical segments. Based on Eq. B1, the combined heterodyne

efficiency for the horizontal segments is given by

$$\eta'_{\text{het,hor}} = \left| \int_0^{R_{\text{min}}} A_{\text{re}} \exp(-i k_s y \sin(M_2 \alpha_{\text{rx}}) \cos(M_2 \beta_{\text{rx}})) dy \right|^2, \quad (\text{B9})$$

with

$$A_{\text{re}} := \frac{1}{2} e^{-y^2/W_0^2} \operatorname{erf}(\sqrt{R_{\text{min}}^2 - y^2}/W_0 - \frac{1}{2} i W_0 k_s \sin(M_2 \beta_{\text{rx}})) - \frac{1}{2} e^{-y^2/W_0^2} \operatorname{erf}(-\sqrt{R_{\text{min}}^2 - y^2}/W_0 - \frac{1}{2} i W_0 k_s \sin(M_2 \beta_{\text{rx}})). \quad (\text{B10})$$

According to Eq. B2,  $A_{\text{re}}$  is real. Performing similar steps as in Eq. B8, the heterodyne efficiency once all four segments are combined is given by

$$\eta'_{\text{het,all}} = \left| \int_0^{R_{\text{min}}} A_{\text{re}} \cos(k_s y \sin(M_2 \alpha_{\text{rx}}) \cos(M_2 \beta_{\text{rx}})) dy \right|^2. \quad (\text{B11})$$

Comparison of Eq. B9 and Eq. B11 then yields  $\eta_{\text{het,hor}} \geq \eta_{\text{het,all}}$ . Due to rotational symmetry of the problem the

statement also holds if instead of the two horizontal segments the two vertical segments are combined. We can summarize that the heterodyne efficiency of two combined adjacent segments outperforms the heterodyne efficiency once all four segments are combined.

Finally, we want to compare the heterodyne efficiency of a single segment to the one of two combined adjacent segments. Therefore, we will introduce the following substitutions

$$\begin{aligned} A_{\text{re}} + iA_{\text{im}} &= -\frac{1}{2}e^{-y^2/W_0^2} \operatorname{erf}\left(-\frac{1}{2}iW_0k_s \sin(M_2\beta_{\text{rx}})\right) \\ &+ \frac{1}{2}e^{-y^2/W_0^2} \operatorname{erf}\left(\sqrt{R_{\text{min}}^2 - y^2}/W_0 - \frac{1}{2}iW_0k_s \sin(M_2\beta_{\text{rx}})\right), \end{aligned} \quad (\text{B12})$$

and

$$B_{\text{re}} + iB_{\text{im}} = \exp(-ik_s y \sin(M_2\alpha_{\text{rx}}) \cos(M_2\beta_{\text{rx}})), \quad (\text{B13})$$

with  $A_{\text{re}}, A_{\text{im}}, B_{\text{re}}, B_{\text{im}} \in \mathbb{R}$ . Note that based on Eq. B3, the definition of  $A_{\text{re}}$  is given in Eq. B10. Expressing the heterodyne efficiency of segment 1 via Eq. B12 and Eq. B13, results in

$$\begin{aligned} \eta'_{\text{het,seg 1}} &= \\ &\left| \int_0^{R_{\text{min}}} A_{\text{re}}(B_{\text{re}} + iB_{\text{im}}) dy + \int_0^{R_{\text{min}}} iA_{\text{im}}(B_{\text{re}} + iB_{\text{im}}) dy \right|^2 \\ &= |C_1 + C_2|^2, \end{aligned}$$

with

$$\begin{aligned} C_1 &= \int_0^{R_{\text{min}}} A_{\text{re}}(B_{\text{re}} + iB_{\text{im}}) dy, \\ C_2 &= \int_0^{R_{\text{min}}} iA_{\text{im}}(B_{\text{re}} + iB_{\text{im}}) dy, \end{aligned}$$

and  $C_1, C_2 \in \mathbb{C}$ . Moreover, we will consider the heterodyne efficiency of segment 4 with  $x^- = -\sqrt{R_{\text{min}}^2 - y^2}$ ,  $x^+ = 0$  and  $y^- = 0$ ,  $y^+ = R_{\text{min}}$ . Based on Eq. B4, it is straightforward to show that

$$\eta'_{\text{het,seg 4}} = |C_1 - C_2|^2.$$

Finally, we note that  $\eta'_{\text{het,hor}}$  as given in Eq. B9 equals  $|C_1|^2$ . Using the inner product to show that

$$|C_1| \leq \max(|C_1 + C_2|, |C_1 - C_2|),$$

we can conclude that  $\eta_{\text{het,hor}} \leq \max(\eta_{\text{het,seg 1}}, \eta_{\text{het,seg 4}})$ . In a similar way it can be shown that  $\eta_{\text{het,ver}} \leq \max(\eta_{\text{het,seg 1}}, \eta_{\text{het,seg 4}})$ . Finally, based on symmetry arguments we have

$$\max(\eta_{\text{het,hor}}, \eta_{\text{het,ver}}) \leq \max(\eta_{\text{het,seg 1}}, \eta_{\text{het,seg 2}}), \quad (\text{B14})$$

and we can conclude that the maximum heterodyne efficiency of the single segments is always greater or equal to the maximum heterodyne efficiency of all possible combinations of two adjacent QPD segments.

## Appendix C: Received power

This appendix investigates the impact of a pointing error of the remote SC on the received power at the local SC. The modeling is performed using the Fraunhofer approximation. This approximation is well suited due to the large distance ( $\approx 2.5 \cdot 10^9$  m) between the SC. The beam leaving the remote SC is modeled as a Gaussian beam and is given at the external Tx pupil as follows [27]

$$\begin{aligned} E_{\text{s}}(x_{\text{s}}, y_{\text{s}}, z_{\text{s}}, t) &= E_{\text{s}}^0 \exp\left(-\frac{x_{\text{s}}^2 + y_{\text{s}}^2}{W_{\text{tx}}^2(z_{\text{s}})}\right) \\ &\cdot \exp\left(ik_{\text{s}}z_{\text{s}} + ik_{\text{s}}\frac{x_{\text{s}}^2 + y_{\text{s}}^2}{2R(z_{\text{s}})} - i\zeta(z_{\text{s}}) - i\omega_{\text{s}}t\right), \end{aligned} \quad (\text{C1})$$

with

$$\begin{aligned} W_{\text{tx}}(z) &= W_{0,\text{tx}}\sqrt{1 + (z/z_0)^2}; \quad R(z) = z[1 + (z_0/z)^2]; \\ \zeta(z) &= \operatorname{atan}(z/z_0); \quad W_0 = \sqrt{\lambda z_0/\pi}. \end{aligned}$$

The beam waist at the Tx aperture  $W_{0,\text{tx}}$  is related to the beam waist at the QPD via  $W_{0,\text{tx}} = W_0 M_2$ , see Fig 1 b). The parameter  $\omega_{\text{s}}$  denotes the angular frequency and  $k_{\text{s}}$  the wave vector. Finally  $z_0$  represents the Rayleigh range. We note that the transmitting beam, i.e. the signal beam, is expressed in its local coordinates  $(x_{\text{s}}, y_{\text{s}}, z_{\text{s}})$ . The power of an unclipped beam is then given by

$$P_{\text{s}'} = \int_A \frac{1}{2} c \epsilon_0 E_{\text{s}} \cdot E_{\text{s}}^* da = \frac{1}{4} \pi c \epsilon_0 W_{\text{tx}}^2(z_{\text{s}}) |E_{\text{s}}^0|^2. \quad (\text{C2})$$

The electric field  $E_{\text{ff}}$  in the far-field is computed in Fraunhofer approximation. The Fraunhofer approximation at a distant  $d_{\text{sc}}$ , i.e.  $z_{\text{s}} = d_{\text{sc}}$ , is given by [27]

$$\begin{aligned} E_{\text{ff}}(x_{\text{s}}, y_{\text{s}}, d_{\text{sc}}, t) &= h_0 \exp(-i\pi(x_{\text{s}}^2 + y_{\text{s}}^2)/\lambda_{\text{s}}/d_{\text{sc}}) \\ &\cdot \iint_{A_{\text{tx}}} E_{\text{s}}(x', y', 0, t) \exp\left(i\frac{2\pi}{\lambda_{\text{s}}d_{\text{sc}}}(x_{\text{s}}x' + y_{\text{s}}y')\right) dx' dy', \end{aligned}$$

with  $h_0 := (i/\lambda_{\text{s}}/d_{\text{sc}}) \exp(-ik_{\text{s}}d_{\text{sc}})$ , where  $\lambda_{\text{s}}$  denotes the wavelength of the signal beam. The subscript  $A_{\text{tx}}$  at the integrals indicates the integration over the limiting aperture at the transmitting SC, which is the aperture with radius  $R_{\text{tel}}$ , see Fig. 1 b). In the following, we will express the field using cylindrical coordinates, i.e.  $E_{\text{ff}}(d_{\text{sc}}, x_{\text{s}}, y_{\text{s}}) \rightarrow E_{\text{ff}}(d_{\text{sc}}, r, \phi)$  and the integral via polar coordinates, considering the following relation:  $x_{\text{s}} = r \cos \phi$ ,  $y_{\text{s}} = r \sin \phi$  and  $x' = r' \cos \phi'$ ,  $y' = r' \sin \phi'$ . Further, using various substitutions we get:

$$\begin{aligned} E_{\text{ff}}(r, \phi, d_{\text{sc}}, t) &= h_0 \exp(-i\pi r^2/\lambda_{\text{s}}/d_{\text{sc}}) \\ &\cdot \iint_{A_{\text{tx}}} E_{\text{s}}(r' \cos \phi', r' \sin \phi', 0, t) e^{i2\pi \frac{rr'}{\lambda_{\text{s}}d_{\text{sc}}} \cos(\phi' - \phi)} d\phi' r' dr'. \\ &= E_{\text{s}}^0 h_0 \exp(-i\pi r^2/\lambda_{\text{s}}/d_{\text{sc}}) \exp(-i\omega_{\text{s}}t) \\ &\cdot \int_0^{R_{\text{tel}}} e^{-(r'/W_{0,\text{tx}})^2} \int_0^{2\pi} e^{i2\pi \frac{rr'}{\lambda_{\text{s}}d_{\text{sc}}} \cos(\phi' - \phi)} d\phi' r' dr' \end{aligned}$$



At this point, we consider the following identity of the zero-order Bessel function of first kind:

$$J_0(x) = \frac{1}{2\pi} \int_{-\pi}^{\pi} e^{i(x \sin \varphi)} d\varphi = \frac{1}{2\pi} \int_{-(n-1)\pi+a}^{(n+1)\pi+a} e^{i(x \sin \varphi)} d\varphi,$$

which is based on the periodicity of the sine. Thus, we have:

$$E_{ff}(r, \phi, d_{sc}, t) = 2\pi E_s^0 h_0 \exp(-i\pi r^2/\lambda_s/d_{sc}) \cdot \exp(-i\omega_s t) \int_0^1 R_{tel}^2 \rho e^{-(\rho R_{tel}/W_{0,tx})^2} J_0\left(\frac{2\pi}{\lambda_s} \frac{r}{d_{sc}} R_{tel} \rho\right) d\rho.$$

Note that the field is circular symmetric around the  $z_s$ -axis and thus independent of  $\phi$ , i.e.  $E_{ff}(r, \phi, d_{sc}, t) = E_{ff}(r, d_{sc}, t)$ . In the following we will express the field via the angle  $\gamma_{tx} := r/d_{sc}$  (paraxial approximation). This angle  $\gamma_{tx}$  may also be regarded as  $\gamma_{tx} = \sqrt{\alpha_{tx}^2 + \beta_{tx}^2}$  following the definition of section II A. We then get

$$E_{ff}(\gamma_{tx}, d_{sc}, t) = i \frac{2\pi}{\lambda_s d_{sc}} E_s^0 \exp(-ik_s d_{sc} - \frac{i\pi r^2}{\lambda_s d_{sc}} - i\omega_{tx} t) \cdot \int_0^1 R_{tel}^2 \rho e^{-(\rho R_{tel}/W_{0,tx})^2} J_0(k_{tx} R_{tel} \varphi_{tx} \rho) d\rho = -\frac{k_s R_{tel}^2}{i d_{sc} r_{tx}} E_s^0 \exp(-ik_s d_{sc} (1 + \gamma_{tx}^2/2 - i\omega_s t)) F(r_{tx}, \kappa_{tx}),$$

with

$$F(r, \kappa) := r \int_0^1 \rho e^{-r^2 \rho^2} J_0(\kappa \rho) d\rho$$

and  $\kappa_{tx} := k_{tx} R_{tel} \gamma_{tx}$ ,  $r_{tx} := R_{tel}/W_{0,tx}$ .

Taking into account Eq. C2, the power at the external Rx pupil  $A_{rx}$  of the local SC with radius  $R_{tel}$  is given by

$$P_{ff}(\gamma_{tx}) = \frac{1}{2} c \epsilon_0 \int_{A_{rx}} |E_{ff}|^2 da = \frac{\pi}{2} R_{tel}^2 c \epsilon_0 |E_{ff}|^2 = 2P_{s'} \left( \frac{k_s R_{tel}^2}{d_{sc}} \right)^2 F^2(r_{tx}, \kappa_{tx}(\gamma_{tx})).$$

Finally, incorporating losses in the on-board transmit and receive path by replacing  $P_{s'}$  with  $P_{s,n}$  the power of the signal beam received at the SC is given by:

$$P_s(\gamma_{tx}) = 2P_{s,n} \left( \frac{k_s R_{tel}^2}{d_{sc}} \right)^2 F^2(r_{tx}, \kappa_{tx}(\gamma_{tx}))$$

Note that we assumed a uniform power distribution over the integration area at the receiving SC based on the large ratio of the distance of the SC to the receiver aperture. This approximation is justified by numerical evaluations, which exhibit a normalized deviation of  $1 - dP_{ff}(R_{tel})/dP_{ff}(0) = 5.1 \cdot 10^{-10}$ , where  $dP_{ff}$  is the received power defined over a circular area with radius  $R_{tel}/1e6$ .

- 
- [1] K. Danzmann, T. A. Prince, *et al.*, *LISA Assessment Study Report (Yellow Book)*, Tech. Rep. ESA/SRE(2011)3 (European Space Agency, 2011).
- [2] F. Cirillo and P. F. Gath, Control system design for the constellation acquisition phase of the LISA mission, *Journal of Physics: Conference Series* **154**, 012014 (2009).
- [3] G. Hechenblaikner, Measurement of the absolute wavefront curvature radius in a heterodyne interferometer, *J. Opt. Soc. Am. A* **27**, 2078–2083 (2010).
- [4] C. Hindman and L. Robertson, Beaconless satellite laser acquisition - modeling and feasibility, in *IEEE MILCOM 2004. Military Communications Conference, 2004.*, Vol. 1 (2004) pp. 41–47 Vol. 1.
- [5] T. T. Hyde, P. G. Maghami, and S. M. Merkwowitz, Pointing acquisition and performance for the laser interferometry space antenna mission, *Classical and Quantum Gravity* **21**, S635 (2004).
- [6] G. Hechenblaikner, Analysis of performance and robustness against jitter of various search methods for acquiring optical links in space, *Appl. Opt.* **60**, 3936–3946 (2021).
- [7] G. Hechenblaikner, Impact of spectral noise shape and correlations of laser beam jitter on acquiring optical links in space, *Appl. Opt.* **61**, 710–720 (2022).
- [8] G. Hechenblaikner, S. Delchambre, and T. Ziegler, Optical link acquisition for the LISA mission with in-field pointing architecture, *Optics & Laser Technology* **161**, 109213 (2023).
- [9] G. Hechenblaikner, Probabilistic model to spatially acquire optical links in space under the influence of band-limited beam jitter, *Appl. Opt.* **62**, 1582–1591 (2023).
- [10] Y. Huang, C. Li, N. Xin, W. Cai, S. Yuan, N. Liu, L. Liu, and Y. Lu, Capture Probability Modeling and Simulation in Satellite-Ground Laser Link under Vibrations, in *2023 IEEE 18th Conference on Industrial Electronics and Applications (ICIEA)* (2023) pp. 352–357.
- [11] R. Gao, H. Liu, Y. Zhao, Z. Luo, and G. Jin, High-precision laser spot center positioning method for weak light conditions, *Appl. Opt.* **59**, 1763–1768 (2020).
- [12] S. Barke, N. Brause, I. Bykov, J. J. Esteban Delgado, A. Enggaard, O. Gerberding, *et al.*, LISA Metrology System - Final Report (2014).
- [13] R. Gao, Y. Wang, Z. Cui, H. Liu, A. Liu, X. Qian, X. Wang, Z. Yao, Q. Yang, J. Jia, K. Qi, S. Wang, Z. Luo, G. Jin, and J. Wang, On-ground demonstration of laser-link construction for space-based detection of gravitational waves, *Optics and Lasers in Engineering* **160**, 107287 (2023).
- [14] E. Morrison, B. J. Meers, D. I. Robertson, and H. Ward, Automatic alignment of optical interferometers, *Appl. Opt.* **33**, 5041–5049 (1994).
- [15] J. J. Esteban, I. Bykov, A. F. G. Marín, G. Heinzel, and K. Danzmann, Optical ranging and data transfer devel-

- opment for LISA, *J. Phys. Conf. Ser.* **154**, 10.1088/1742-6596/154/1/012025 (2009), Art. no. 012025.
- [16] G. Heinzel, J. J. Esteban, S. Barke, M. Otto, Y. Wang, A. F. Garcia, and K. Danzmann, Auxiliary functions of the LISA laser link: ranging, clock noise transfer and data communication, *Class. Quantum Gravity* **28** (2011), Art. no. 094008.
- [17] P. Euringer, G. Hechenblaikner, F. Soualle, and W. Fichter, Performance Analysis of Sequential Carrier- and Code-Tracking Receivers in the Context of High-Precision Spaceborne Metrology Systems, *IEEE Transactions on Instrumentation and Measurement* **73**, 1–10 (2024).
- [18] N. C. Brause, *Auxiliary function development for the LISA metrology system*, Ph.D. thesis, Gottfried Wilhelm Leibniz Universität (2018).
- [19] F. Ales, O. Mandel, P. Gath, U. Johann, and C. Braxmaier, A phasemeter concept for space applications that integrates an autonomous signal acquisition stage based on the discrete wavelet transform, *Rev. Sci. Instrum.* **86**, 10.1063/1.4928489 (2015), Art. no. 084502.
- [20] Z. Wang, T. Yu, Y. Sui, and Z. Wang, Beat-Notes Acquisition of Laser Heterodyne Interference Signal for Space Gravitational Wave Detection, *Sensors* **23**, 10.3390/s23063124 (2023).
- [21] Q.-T. Zhang, H.-S. Liu, P. Dong, P. Li, and Z.-R. Luo, Multi-frequency signal acquisition and phase measurement in space gravitational wave detection, *Review of Scientific Instruments* **95**, 054501 (2024).
- [22] G. Wanner, G. Heinzel, E. Kochkina, C. Mahrtdt, B. S. Sheard, S. Schuster, and K. Danzmann, Methods for simulating the readout of lengths and angles in laser interferometers with Gaussian beams, *Optics Communications* **285**, 4831–4839 (2012).
- [23] G. Wanner and G. Heinzel, Analytical description of interference between two misaligned and mismatched complete Gaussian beams, *Appl. Opt.* **53**, 3043–3048 (2014).
- [24] C. Mahrtdt, *Laser link acquisition for the GRACE follow-on laser ranging interferometer*, Ph.D. thesis, Gottfried Wilhelm Leibniz Universität Hannover (2014).
- [25] LISA Consortium, *LISA Performance Model and Error Budget*, Tech. Rep. (2021) LISA-LCST-INST-TN-003. Technical Report 2.1, ESA.
- [26] B. Bachman, G. de Vine, J. Dickson, S. Dubovitsky, J. Liu, W. Klipstein, K. McKenzie, R. Spero, A. Sutton, B. Ware, and C. Woodruff, Flight phasemeter on the Laser Ranging Interferometer on the GRACE Follow-On mission, *Journal of Physics: Conference Series* **840**, 012011 (2017).
- [27] B. E. A. Saleh and M. C. Teich, *Fundamentals of photonics; 3rd edition* (Wiley, Hoboken, 2019).
- [28] G. Heinzel, M. D. Álvarez, A. Pizzella, N. Brause, and J. J. E. Delgado, Tracking Length and Differential-Wavefront-Sensing Signals from Quadrant Photodiodes in Heterodyne Interferometers with Digital Phase-Locked-Loop Readout, *Phys. Rev. Appl.* **14**, 054013 (2020).
- [29] J. J. Esteban Delgado, *Laser Ranging and Data Communication for the Laser Interferometer Space Antenna*, Ph.D. thesis, Universidad de Granada (2012).
- [30] E. Fitzsimons, *LISA Tilt-to-Length and Optical Alignment Analysis*, Tech. Rep. (2019) LISA-UKOB-INST-TN-004.
- [31] A. Sutton, K. McKenzie, B. Ware, and D. A. Shaddock, Laser ranging and communications for LISA, *Opt. Express* **18**, 20759–20773 (2010).
- [32] L. Wissel, A. Wittchen, T. S. Schwarze, M. Hewitson, G. Heinzel, and H. Halloin, Relative-Intensity-Noise Coupling in Heterodyne Interferometers, *Phys. Rev. Appl.* **17**, 024025 (2022).
- [33] L. Wissel, O. Hartwig, J. Bayle, M. Staab, E. Fitzsimons, M. Hewitson, and G. Heinzel, Influence of Laser Relative-Intensity Noise on the Laser Interferometer Space Antenna, *Phys. Rev. Appl.* **20**, 014016 (2023).
- [34] G. Fernández Barranco, *Photodetection in intersatellite laser interferometers*, Ph.D. thesis, Gottfried Wilhelm Leibniz Universität Hannover (2017).
- [35] G. Hechenblaikner, V. Wand, M. Kersten, K. Danzmann, A. García, G. Heinzel, M. Nofrarias, and F. Steier, Digital Laser Frequency Control and Phase-Stabilization Loops in a High Precision Space-Borne Metrology System, *IEEE Journal of Quantum Electronics* **47**, 651–660 (2011).
- [36] G. Hechenblaikner, R. Gerndt, U. Johann, P. Luetzow-Wentzky, V. Wand, H. Audley, K. Danzmann, A. Garcia-Marin, G. Heinzel, M. Nofrarias, and F. Steier, Coupling characterization and noise studies of the optical metrology system onboard the LISA Pathfinder mission, *Appl. Opt.* **49**, 5665–5677 (2010).
- [37] G. Fernández Barranco, B. S. Sheard, C. Dahl, W. Mathis, and G. Heinzel, A Low-Power, Low-Noise 37-MHz Photoreceiver for Intersatellite Laser Interferometers Using Discrete Heterojunction Bipolar Transistors, *IEEE Sens. J.* **18**, 7414–7420 (2018).
- [38] G. Heinzel, A. Rüdiger, and R. Schilling, Spectrum and spectral density estimation by the Discrete Fourier transform (DFT), including a comprehensive list of window functions and some new at-top windows (2002).
- [39] B. Quinn, Estimating frequency by interpolation using Fourier coefficients, *IEEE Transactions on Signal Processing* **42**, 1264–1268 (1994).
- [40] F. Harris, On the use of windows for harmonic analysis with the discrete Fourier transform, *Proceedings of the IEEE* **66**, 51–83 (1978).
- [41] X.-G. Xia, Discrete chirp-Fourier transform and its application to chirp rate estimation, *IEEE Transactions on Signal Processing* **48**, 3122–3133 (2000).
- [42] K. Yamamoto, I. Bykov, J. N. Reinhardt, C. Bode, P. Grafe, M. Staab, N. Messied, M. Clark, G. Fernández Barranco, T. S. Schwarze, O. Hartwig, J. J. Esteban Delgado, and G. Heinzel, Experimental end-to-end demonstration of intersatellite absolute ranging for LISA (2024), arXiv:2406.03074.
- [43] S. Xie, H. Zeng, Y. Pan, D. He, S. Jiang, Y. Li, Y. Du, H. Yan, and H. chi Yeh, Bi-directional PRN laser ranging and clock synchronization for TianQin mission, *Optics Communications* **541**, 129558 (2023).
- [44] H. Zeng, H. Yan, S. Xie, S. Jiang, Y. Li, Y. Pan, D. He, Y. Du, and H. chi Yeh, Experimental demonstration of weak-light inter-spacecraft clock jitter readout for TianQin, *Opt. Express* **31**, 34648–34666 (2023).
- [45] M. Xu, Y. Tan, H. Wu, P. Wang, H. Yan, Y. Liang, and C. Shao, Influence of EOM sideband modulation noise on space-borne gravitational wave detection, *Results in Physics* **57**, 107366 (2024).
- [46] J. J. Esteban, A. F. García, S. Barke, A. M. Peinado, F. G. Cervantes, I. Bykov, G. Heinzel, and K. Danz-

- mann, Experimental demonstration of weak-light laser ranging and data communication for LISA, *Opt. Express* **19**, 15937–15946 (2011).
- [47] K. Yamamoto, C. Vorndamme, O. Hartwig, M. Staab, T. S. Schwarze, and G. Heinzel, Experimental verification of intersatellite clock synchronization at LISA performance levels, *Phys. Rev. D* **105**, 042009 (2022).
- [48] F. M. Gardner, *Phaselock Techniques*, 3rd ed. (John Wiley & Sons, Inc., Hoboken, New Jersey, 2005).
- [49] W. B. Davenport and W. L. Root, *An introduction to the theory of random signals and noise* (IEEE Press, New York, 1987).
- [50] H. So, Y. Chan, Q. Ma, and P. Ching, Comparison of various periodograms for sinusoid detection and frequency estimation, *IEEE Transactions on Aerospace and Electronic Systems* **35**, 945–952 (1999).
- [51] R. N. McDonough and A. D. Whalen, *Detection of Signals in Noise*, 2nd ed. (Academic Press, 1995).
- [52] D. Rife and R. Boorstyn, Single tone parameter estimation from discrete-time observations, *IEEE Transactions on Information Theory* **20**, 591–598 (1974).
- [53] C. Helstrom, Computing the generalized Marcum Q-function, *IEEE Transactions on Information Theory* **38**, 1422–1428 (1992).
- [54] A. Steinhardt and C. Bretherton, Thresholds in frequency estimation, in *ICASSP '85. IEEE International Conference on Acoustics, Speech, and Signal Processing*, Vol. 10 (1985) pp. 1273–1276.
- [55] D. S. Elliott, R. Roy, and S. J. Smith, Extracavity laser band-shape and bandwidth modification, *Phys. Rev. A* **26**, 12–18 (1982).
- [56] M. Otto, Time-delay interferometry simulations for the laser interferometer space antenna (2015).
- [57] J. Cooley and J. Tukey, An Algorithm for the Machine Calculation of Complex Fourier Series, *Mathematics of Computation* **19**, 297–301 (1965).
- [58] M. R. Zaghoul and A. N. Ali, Algorithm 916: Computing the Faddeyeva and Voigt Functions, *ACM Trans. Math. Softw.* **38**, 10.1145/2049673.2049679 (2012).